



Direct conversion of furfural to 1,5-pentanediol over a nickel–cobalt oxide–alumina trimetallic catalyst

Rizky Gilang Kurniawan^a, Neha Karanwal^b, Jaeyong Park^c, Deepak Verma^{a,b,c}, Sang Kyu Kwak^d, Seok Ki Kim^e, Jaehoon Kim^{a,b,c,*}

^a School of Chemical Engineering, Sungkyunkwan University, 2066 Seobu-Ro, Jangan-Gu, Suwon, Gyeong Gi-Do 16419, Republic of Korea

^b SKKU Advanced Institute of Nanotechnology (SAINT), Sungkyunkwan University, 2066 Seobu-Ro, Jangan-Gu, Suwon, Gyeong Gi-Do 16419, Republic of Korea

^c School of Mechanical Engineering, Sungkyunkwan University, 2066 Seobu-Ro, Jangan-Gu, Suwon, Gyeong Gi-Do 16419, Republic of Korea

^d School of Energy and Chemical Engineering, Ulsan National Institute of Science and Technology, Ulsan 44919, Republic of Korea

^e Department of Chemical Engineering, Ajou University, Suwon 16499, Republic of Korea

ARTICLE INFO

Keywords:

Furfural

1

5-Pentanediol

Direct conversion

Nickel

Cobalt

Oxygen vacancy

ABSTRACT

The use of a Ni–CoO_x–Al₂O₃ mixed metal–metal oxide catalyst was proposed for the one-pot direct conversion of furfural (FFA) to 1,5-pentanediol (1,5-PDO), which afforded a high yield (47.5%) at 160 °C and at an initial H₂ pressure of 3 MPa for 6 h in ethanol. Proximity between the Ni⁰ and oxygen-vacant CoO_x (O_v–CoO_x) sites favored the dissociative adsorption of H₂ molecules on Ni⁰ and subsequent hydrogen spillover to O_v–CoO_x. The hydrogenation of the C=O group of FFA produced furfuryl alcohol, which was then adsorbed on the Co^{δ+} center of the O_v–CoO_x site in a η¹–(O)–alcoholic configuration, where subsequent C–O bond cleavage produced 1,5-PDO. Catalytic activity loss through the oxidation of the Ni⁰ and O_v sites could be mitigated by reactivation under H₂. Thus, the developed Ni–CoO_x–Al₂O₃ catalyst has potential for efficient, low-cost, and environmentally friendly 1,5-PDO production from FFA.

1. Introduction

Lignocellulosic biomass is abundantly available, inexpensive and can be used to produce a variety of useful compounds. Thus, the conversion of lignocellulosic biomass to biofuels and value-added platform chemicals is a promising approach for developing sustainable chemical processes [1,2]. Furfural (FFA), a key renewable intermediate produced by the acid-catalyzed transformation of C₅ sugars in lignocellulosic biomass, can be hydrogenated to obtain a variety of high-value products (Fig. 1) [3]. For example, the selective hydrogenation of the C=O bond in FFA produces furfuryl alcohol (FOL) and the subsequent hydrogenolysis of the C–OH bond in FOL gives 2-methylfuran (2-MF), which can be used as a second-generation biofuel. In addition, the saturation of the furan ring in FFA results in tetrahydrofurfuryl alcohol (THFOL), which can be used in electronic cleaners, inks, and agriculture applications [3,4]. FFA ring opening via C–O–C bond cleavage and subsequent C=C bond hydrogenation produce 1,5-pentanediol (1,5-PDO) and 1,2-pentanediol (1,2-PDO) [5,6]. Notably, 1,5-PDO is among the most valuable chemicals, with a global market value of USD 28 million in

2020 that is expected to reach USD 42 million by the end of 2027 [7]. Currently, 1,5-PDO is used as a building block for the synthesis of polyesters and polyurethanes, a solvent for inkjet ink formulations, and an ingredient in solvent-borne paint formulations [6].

Various types of catalysts have been applied to synthesize 1,5-PDO from biomass-derived feedstocks such as FFA, FOL, and THFOL (for selected examples, see Table S1). In the multistep reaction routes from lignocellulosic biomass to 1,5-PDO, separation/purification after each reaction step is time consuming and highly energy intensive. Thus, the one-pot direct conversion of FFA to 1,5-PDO is highly desirable. However, this approach requires several consecutive reaction steps and the suppression of competing reactions, which impede the achievement of 1,5-PDO in a high yield. For THFOL conversion to 1,5-PDO, a widely recognized catalyst design strategy involves placing a hydrogenation-active metallic site (e.g., Rh, Ir, and Pt) in close proximity to an oxophilic site (e.g., ReO_x, MoO_x, and WO_x) to achieve desirable adsorption geometries and reaction pathways [8–19]. Over such metal–oxophilic bimetallic catalysts, THFOL conversion proceeds by a regioselective hydride attack mechanism (Fig. S1a) [10]. In this mechanism, the –OH

* Correspondence to: School of Chemical Engineering, School of Mechanical Engineering, and SKKU Advanced Institute of Nanotechnology, Sungkyunkwan University, 2066 Seobu-Ro, Jangan-Gu, Suwon, Gyeong Gi-Do 16419, Republic of Korea.

E-mail address: jaehoonkim@skku.edu (J. Kim).

<https://doi.org/10.1016/j.apcatb.2022.121971>

Received 12 July 2022; Received in revised form 22 August 2022; Accepted 7 September 2022

Available online 9 September 2022

0926-3373/© 2022 Elsevier B.V. All rights reserved.

group of THFOL is adsorbed on the oxophilic site by dehydration and H^+ is adsorbed on the metallic site by heterolytic H_2 cleavage. H^- attack at the C_2 atom of THFOL leads to ring opening, and the obtained alkoxide species then reacts with a proton to produce 1,5-PDO. For this conversion, the 1,5-PDO yield is highly dependent on the choice of metal and oxophilic sites, reaching up to 94.0% over the Rh– ReO_x /C catalyst [16] and as low as 1.68% over the 4% Ru– MoO_x /SiO₂ catalyst [13]. Later, a new multistep dehydration, hydration, and hydrogenation pathway was introduced for the conversion of FFA to 1,5-PDO (Fig. S1b) [6,20,21]. First, FFA hydrogenation over a Ni-based catalyst (e.g., Ni/SiO₂, Ni–Al, Ni–Co–Al, and Ni–Mg–Al) produces THFOL, which is then dehydrated over γ -Al₂O₃ in the gas phase to produce 3,4-dihydro-2H-pyran (DHP). Subsequently, DHP hydration in the absence of a catalyst gives 2-hydroxytetrahydropyran (2-HY-THP), which is converted to 5-hydroxyvaleraldehyde (5-HY-Val) by ring-opening tautomerization over 5 wt% Ru/C or 1 wt% Ru/TiO₂. Finally, 5-HY-Val hydrogenation over 5 wt% Ru/C or 1 wt% Ru/TiO₂ results in 1,5-PDO. Via this route, the yield of 1,5-PDO from THFOL reaches up to 80.6% (Table S1) [20].

In contrast to these multistep routes, only a few studies have been dedicated to the direct conversion of FFA to 1,5-PDO (Table S1). For example, Xu et al. converted FFA directly to 1,5-PDO (34.9% yield) over a Li-modified Pt/Co₂AlO₄ catalyst at 140 °C and 1.5 MPa H_2 for 24 h in ethanol [5]. Gavilá et al. performed direct FFA conversion to 1,5-PDO (30.0% yield) over a Co–Al catalyst at 150 °C and 3 MPa H_2 for 8 h in isopropyl alcohol [22]. Sulmonetti et al. converted FFA to 1,5-PDO (33% yield) over Cu–Co–Al at 140 °C and 4 MPa H_2 for 8 h in ethanol [23]. In addition, two-step reactions over trimetallic Rh–Ir– ReO_x /SiO₂ [24] and Pd–Ir– ReO_x /SiO₂ [25] catalysts were proposed to produce 1,5-PDO in a high yield. These two-step reactions, involving FFA hydrogenation to THFOL at 40–60 °C for 2 h followed by THFOL hydrogenolysis to 1,5-PDO at 100–120 °C for 24–48 h, afforded higher 1,5-PDO yields (63.8–71.1%) than those through the corresponding one-pot processes.

Thus, the direct conversion of FFA to 1,5-PDO over a heterogeneous catalyst remains a great challenge, and various issues should be addressed, as follows. (1) Although 1,5-PDO can be produced in a high yield via multistep routes, additional highly energy-intensive, time-consuming, and expensive separation techniques must be applied to recover reaction intermediates (e.g., FOL and THFOL), solvents, and spent catalysts. (2) The high costs of noble metals and oxophilic metal oxides (e.g., Rh: 450.11 USD g^{−1} [26], Ir: 193.50 USD g^{−1} [27], and Re: 1.73 USD g^{−1}) [28] hinder the practical-scale implementation of renewable 1,5-PDO production. However, the use of non-noble-metal-based catalysts for the one-pot direct conversion of FFA

to 1,5-PDO results in relatively low yields (23.9–33.0%, Table S1) [22, 23,29]. (3) In some cases, harsh reaction conditions, such as high H_2 pressures (6–8 MPa) and long reaction times (8–24 h), are required for THFOL ring opening (Table S1) [8–10,15–17,25,30,31], which increase 1,5-PDO production costs. (4) The chemoselective synthesis of 1,5-PDO is highly dependent on the adsorption geometries of FFA and its intermediates as well as the sequence of hydrogenation and ring opening [10,22,23]. Therefore, it is desirable to develop an economically feasible non-noble-metal-based catalyst for the one-pot conversion of FFA to 1,5-PDO under mild conditions in an environmentally friendly solvent. Moreover, to design a highly efficient catalyst, an in-depth understanding of the proximity effect between the adsorption and hydrogenation sites is essential.

Herein, we demonstrate that 1,5-PDO can be produced in a high yield via the direct conversion of FFA over a trimetallic Ni–CoO_x–Al₂O₃ mixed metal–metal oxide catalyst in ethanol. The reaction at 160 °C and 3 MPa H_2 for 6 h gives a 1,5-PDO yield of 47.5%, which is higher than those reported for previous non-noble-metal-based catalysts (Table S1). The trimetallic Ni–CoO_x–Al₂O₃ mixed metal–metal oxide catalyst was designed based on the following rationale: (1) amorphous alumina suppresses Ni⁰ particle growth, which hinders THFOL formation, (2) dissociative H_2 adsorption is favored on Ni⁰ sites with subsequent hydrogen spillover to neighboring CoO_x sites, (3) FFA and FOL can be strongly adsorbed on the Co^{δ+} center of oxygen-vacant CoO_x (O_v–CoO_x) sites, (4) C₂–O bond cleavage on O_v–CoO_x sites is both kinetically and thermodynamically favorable, and (5) starting materials are much cheaper compared to the noble metal and oxophilic metal oxides (Ni: 0.0215 USD kg^{−1}, Co: 0.0605 USD g^{−1}, and Al: 0.0025 USD kg^{−1}) [32]. In this study, the synthesized catalysts were characterized, the reaction conditions were optimized, and reaction mechanisms, catalyst deactivation mechanisms, and catalyst reactivation were evaluated. To obtain further insights into the reaction mechanisms and the role of O_v sites, density functional theory (DFT) calculations were employed.

2. Experimental section

2.1. Materials

Nickel(II) nitrate hexahydrate (Ni(NO₃)₂·6H₂O, > 99% purity), aluminum nitrate nonahydrate (Al(NO₃)₃·9H₂O, > 99% purity), sodium hydroxide (NaOH, >97% purity), sodium carbonate (Na₂CO₃, >99.5% purity), FFA (98% purity), FOL (98% purity), THFOL (98% purity), 1,5-PDO (98% purity), 1,2-PDO (98% purity), 1-pentanol (1-PeOH, 98%

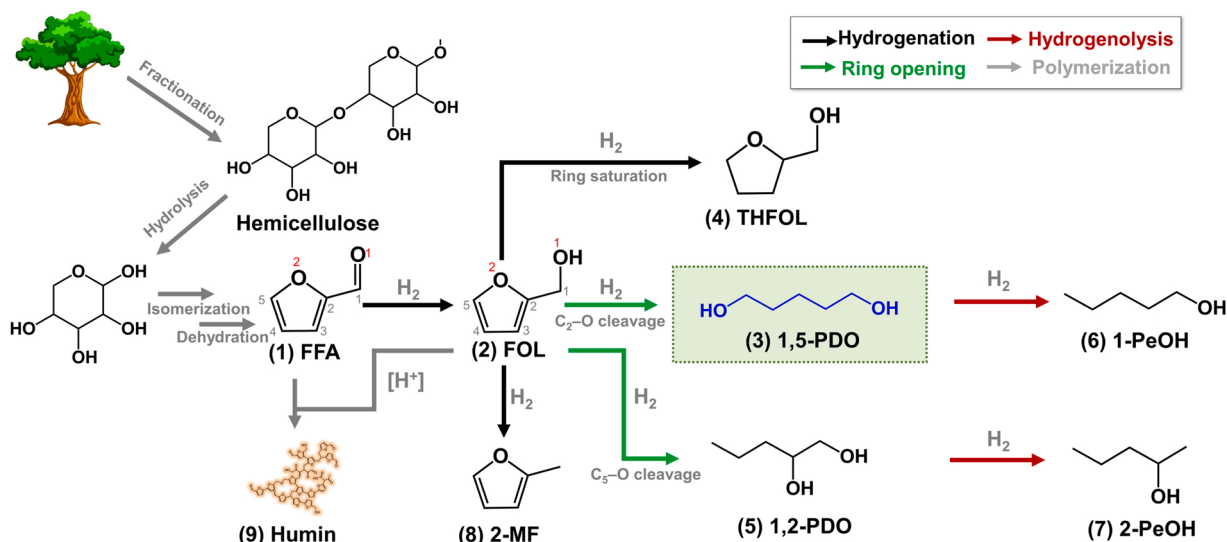


Fig. 1. Reaction pathways for FFA conversion to 1,5-PDO and other competing reactions.

purity), 2-pentanol (2-PeOH, 98% purity), and dodecane were purchased from Alfa Aesar (USA). Cobalt(II) nitrate hexahydrate ($\text{Co}(\text{NO}_3)_2 \cdot 6\text{H}_2\text{O}$, > 99% purity), urea (>99% purity), ammonium carbonate ($(\text{NH}_4)_2\text{CO}_3$, > 30% NH_3 basis), and CoO (325 mesh) were purchased from Sigma-Aldrich (USA). Methanol (99.9% purity) was purchased from Samchun Chemical (Republic of Korea). Ethanol (99.9% purity) was obtained from Honeywell Burdick & Jackson (USA). $\gamma\text{-Al}_2\text{O}_3$ was purchased from Thermo Scientific (USA). All chemicals were used without further purification. Distilled and deionized (DDI) water was produced using an EXL® 7 S Analysis water purification system equipped with a 0.22 μm filter (Vivagen Co., Ltd., Republic of Korea).

2.2. Catalyst synthesis

Trimetallic Ni–CoO_x–Al₂O₃ catalysts with different Ni:Co:Al ratios were synthesized using a coprecipitation method. In a typical synthesis, the required amounts of $\text{Ni}(\text{NO}_3)_2 \cdot 6\text{H}_2\text{O}$, $\text{Co}(\text{NO}_3)_2 \cdot 6\text{H}_2\text{O}$, and Al (NO_3)₃·9H₂O were dissolved in 326 mL of DDI water with a total metal precursor concentration of 0.113 M. The pH of the solution was maintained at 10 ± 0.1 via the dropwise addition of 300 mL of a 0.1 M NaOH and 0.2 M Na₂CO₃ mixture at 25 °C over 30 min under stirring at 400 rpm. After the produced suspension was aged at 80 °C for 24 h, the precipitate was collected by centrifugation, washed with DDI water until the pH reached approximately 7, and dried overnight in a drying oven at 80 °C. The obtained catalyst precursor was calcined under an air flow (80 mL min^{−1}) at 450 °C for 4 h with a heating rate of 4 °C min^{−1}. The calcined sample was then reduced under a 5% H₂/Ar flow (80 mL min^{−1}) at 450 °C for 4 h at a heating rate of 4 °C min^{−1}. The synthesized catalyst was denoted N_xC_yA_z(a:b)-OR, where N represents Ni, C represents Co, A represents Al, x, y, and z represent the Ni:Co:Al mass ratio, a:b represents the NaOH:Na₂CO₃ molar ratio in the precipitate solution, and OR represents oxidation followed by reduction.

Ni–Co–Al catalysts were also synthesized by directly reducing the catalyst precursors under a 5% H₂/Ar flow (80 mL min^{−1}) at 400 °C for 4 h at a heating rate of 4 °C min^{−1} (denoted N_xC_yA_z(a:b)-R, where R represents reduction). For comparison, bimetallic Co–Al (denoted C_xA_y(1:2)-OR), Ni–Al (denoted N_xA_y(1:2)-OR), and Ni–Co (denoted N_xC_y(1:2)-OR) catalysts as well as amorphous monometallic Al₂O₃, Co₃O₄, and NiO catalysts were synthesized via the same method as that used for the synthesis of N_{4.5}C_{3.5}A₁(1:2)-OR, using only the relevant metal precursor(s). To examine the effect of the NaOH and Na₂CO₃ coprecipitant solution on the catalyst performance, catalysts were synthesized using only NaOH (denoted N_xC_yA_z(1:0)-OR) or Na₂CO₃ (denoted N_xC_yA_z(0:1)-OR) as a precipitant. In addition, 20 wt% Ni/ $\gamma\text{-Al}_2\text{O}_3$, 15 wt% Co/ $\gamma\text{-Al}_2\text{O}_3$, and 20 wt% Ni–15 wt% Co/ $\gamma\text{-Al}_2\text{O}_3$ catalysts were synthesized using a wet impregnation method. After impregnation, the dried sample was calcined in an air flow (80 mL min^{−1}) at 450 °C for 4 h at a heating rate of 4 °C min^{−1} and then reduced under a 5% H₂/Ar flow (80 mL min^{−1}) at 450 °C for 4 h.

2.3. Catalyst characterization

X-ray diffraction (XRD) patterns ($2\theta = 3\text{--}90^\circ$; scanning speed: $0.05^\circ \text{ s}^{-1}$) were collected using a high-power powder X-ray diffractometer (D/Max-2500 V/PC, Rigaku, Japan) using Cu-K α ($\lambda = 1.5418 \text{ \AA}$) and Ni foil filtered radiation at 40 kV and 50 mA. The chemical composition of the catalysts was analyzed by X-ray photoelectron spectroscopy (XPS; ESCALAB250, Thermo Scientific, UK) with an Al K α (1486.7 eV) X-ray source. Prior to analysis, freshly reduced catalysts were stored under inert conditions to suppress the formation of native oxides upon exposure to air. All XPS peaks were referenced to the C 1 s peak at 284.8 eV. The Ni, Co, and Al contents of the catalysts were quantitatively determined using inductively coupled plasma optical emission spectroscopy (ICP-OES; 730-ES, Varian, USA). Co and Ni K-edge X-ray absorption spectroscopy (XAS) was performed in the transmission mode at the 8 C beamline of the Pohang Accelerator Laboratory

using a Si (111) double crystal monochromator. For energy calibration, the reference spectra of Co, CoO, and Co₃O₄ powders were obtained simultaneously. X-ray absorption near edge structure (XANES) and extended X-ray absorption fine structure (EXAFS) data were processed using the Athena/Artemis software packages. To highlight high-energy oscillations, the extracted EXAFS data ($\chi(k)$) was weighted by k^3 . To obtain the magnitude of the EXAFS spectra in *R* space, Fourier transform was performed in the *k*-range of 3.0–10.0 \AA^{-1} by applying a Hanning window function.

The textural properties of the catalysts were evaluated on the basis of N₂ adsorption–desorption isotherms collected at -196°C using a Bel-sorp mini II apparatus (BEL Inc., Japan). Prior to analysis, each catalyst was pretreated at 150 °C for 4 h under vacuum using a BELPREP-vac II vacuum degasser (BEL Inc., Japan) to remove trapped moisture and other volatile species. The specific surface area was calculated using the multipoint Brunauer–Emmett–Teller (BET) method, and the average pore diameter (D_p , nm) and pore size distribution were calculated via the Barrett–Joyner–Halenda (BJH) method. The morphologies of the catalysts were observed through field-emission scanning electron microscopy (FE-SEM; Hitachi S-4100, Japan) and Cs-corrected scanning transmission electron microscopy (STEM; Titan 80–300, FEI, USA) equipped with a fast CCD camera (Gatan, Oneview 1095). Elemental mapping analyses were performed through high-resolution transmission electron microscopy (HR-TEM; FEI Talos F200X, USA) coupled with energy-dispersive X-ray spectrometry (EDX; Super-X EDX, Bruker, USA) conducted at 200 keV.

The temperature-programmed desorption of hydrogen (H₂-TPD) was performed using a BELCAT-M instrument (BET Inc., Japan) equipped with a thermal conductivity detector. Prior to H₂ adsorption, a quartz sample tube containing 0.05 g of catalyst was purged with ultrahigh-purity Ar (99.999%, JC Gas Company, Republic of Korea) at a flow rate of 30 mL min^{−1} at 400 °C for 1 h at a heating rate of 5 °C min^{−1}. Subsequently, the catalyst was reduced at 400 °C under ultrahigh-purity 5% H₂/Ar (JC Gas Company) at a flow rate of 30 mL min^{−1} for 1 h. After cooling naturally to 50 °C, the catalyst was completely saturated with 5% H₂/Ar at a flow rate of 30 mL min^{−1} for 30 min. Then, the system was purged with Ar at a flow rate of 30 mL min^{−1} for 30 min at 50 °C to remove physically adsorbed H₂ molecules. Finally, H₂-TPD analysis was performed by increasing the temperature of the sample to 950 °C at a heating rate of 5 °C min^{−1} under an Ar flow (30 mL min^{−1}), and effluent gases were analyzed using quadrupole mass spectrometry (QMS; Transpector® CPM 3, Inficon Inc., USA).

The temperature-programmed desorption of oxygen (O₂-TPD) was also performed using the BELCAT-M instrument. A quartz sample tube containing 0.05 g of catalyst was purged with ultrahigh-purity He (99.999%, JC Gas Company) at a flow rate of 30 mL min^{−1} at 400 °C for 1 h at a heating rate of 10 °C min^{−1}. Then, the catalyst was reduced at 400 °C under 5% H₂/Ar at a flow rate of 30 mL min^{−1} for 1 h. The sample was naturally cooled to 30 °C under a He flow (30 mL min^{−1}) and then purged with He for an additional 30 min at 30 °C. Subsequently, the sample was exposed to O₂ (0.05 mol mol^{−1}, JC Gas Company) at a flow rate of 30 mL min^{−1} for 1 h at 30 °C. After purging with He at a flow rate of 30 mL min^{−1} for 45 min at 30 °C to remove physically adsorbed O₂ molecules, O₂-TPD analysis was performed by increasing the temperature to 950 °C at a heating rate of 10 °C min^{−1} under a He flow (30 mL min^{−1}) to desorb O₂ from the catalyst surface, and effluent gases were analyzed by QMS (Transpector® CPM 3).

The reduction properties of the calcined catalysts were analyzed through the temperature-programmed reduction of hydrogen (H₂-TPR; BELCAT-M). Prior to H₂ adsorption, a quartz sample tube containing 0.05 g of catalyst was heated to 400 °C at a heating rate of 10 °C min^{−1} under an Ar flow (50 mL min^{−1}) and then maintained at 400 °C for 1 h to remove any adsorbed water or volatile species. After cooling naturally to 50 °C, H₂-TPR analysis was performed by increasing the temperature to 1000 °C at a heating rate of 10 °C min^{−1} under a 5% H₂/Ar flow (30 mL min^{−1}).

Catalyst acidity was evaluated using the temperature-programmed desorption of ammonia (NH₃-TPD; BELCAT-M). Prior to NH₃ adsorption, 0.05 g of catalyst was pretreated at 400 °C (heating rate: 10 °C min⁻¹) under a He flow (50 mL min⁻¹) for 1 h and then reduced at 400 °C under a 5% H₂/Ar flow (30 mL min⁻¹) for 1 h. After naturally cooling to 100 °C, the sample was exposed to 5% NH₃/He (99.995%, JC Gas Company) at a flow rate of 30 mL min⁻¹ for 1 h to saturate the catalyst completely. The system was then flushed with ultrahigh-purity He (99.995%, JC Gas Company) at a flow rate of 30 mL min⁻¹ for 30 min to remove any physisorbed NH₃ molecules. NH₃-TPD analysis was performed by increasing the temperature from 100° to 1000 °C at a heating rate of 10 °C min⁻¹ under a He flow (30 mL min⁻¹), and effluent gases were analyzed by QMS (Transpector® CPM 3).

To evaluate the acidic nature of the catalysts, the pyridine-adsorbed diffuse reflectance infrared Fourier transform (pyridine-DRIFT) spectra of the catalysts were collected using a Frontier spectrometer (PerkinElmer, USA) equipped with a mercury cadmium telluride detector and a Praying Mantis cell (Harrick, USA). The catalyst was mixed with KBr at a weight ratio of 1:20. After loading the catalyst into the DRIFT cell, the temperature was increased to 400 °C at a heating rate of 10 °C min⁻¹ under a N₂ flow (10 mL min⁻¹) and then maintained at 400 °C for 1 h. After cooling to 30 °C using a chiller (HTRC-30, JEIO Tech., Republic of Korea), the system was flushed with N₂ for 30 min and background spectra were collected. The sample was subsequently exposed to a pyridine flow by purging a pyridine container with N₂ at a flow rate of 10 mL min⁻¹ for 45 min at 30 °C. The cell was subsequently flushed with N₂ at a flow rate of 10 mL min⁻¹ for 30 min. Residual gaseous species and physisorbed pyridine were removed under vacuum at 0.08 MPa and 30 °C for 30 min. Subsequently, DRIFT spectra were recorded as the temperature was increased to 150 °C at a heating rate of 5 °C min⁻¹.

CO-DRIFT analysis was performed to characterize the active sites. The catalyst was mixed with KBr at a weight ratio of 1:20. After loading in the DRIFT cell, the catalyst was reduced at 400 °C (heating rate: 10 °C min⁻¹) and 0.1 MPa under a H₂ flow (10 mL min⁻¹) for 1 h. Then, the cell was flushed with N₂ at a flow rate of 10 mL min⁻¹ for 30 min and then cooled to 30 °C under a N₂ flow (10 mL min⁻¹) using the chiller. After purging the cell with N₂ for 30 min, background spectra were recorded. The cell was then pressurized using CO/He (0.05 mol mol⁻¹) at a flow rate of 10 mL min⁻¹ for 30 min. Finally, the gas flow was switched to N₂ (10 mL min⁻¹) and CO-DRIFT spectra were recorded during flushing at 30 °C over 30 min.

To investigate thermal stability of and coke formation on the fresh and spent catalysts, thermogravimetric analysis (TGA) was carried out using a Q50 thermogravimetric analyzer (TA Instruments, USA). Prior to TGA analysis, the catalysts were dried in a vacuum oven at 80 °C for overnight. The dried catalyst was loaded to the TGA chamber and purged with N₂ during the temperature ramping to 150 °C at a rate of 2 °C min⁻¹ and the temperature was maintained at 150 °C for 2 h under a N₂ flow condition at 60 mL min⁻¹ to evaporate physisorbed water or other volatile species. After decreasing the temperature to 30 ± 2 °C under a N₂ flow, the gas flow was switched to air (60 mL min⁻¹) and the TGA profile was obtained by increasing the temperature from 30° to 800 °C at a heating rate of 2 °C min⁻¹.

2.4. Catalytic activity and product analysis

FFA conversion was performed in a 140 mL stainless steel batch reactor with a magnetically driven stirrer. A detailed description of the reaction setup can be found elsewhere [33]. In a typical experiment, 0.2 g of FFA, 0.1 g of catalyst, and 40 mL of ethanol were added to the reactor. The reactor was sealed, purged three times with H₂, and then pressurized to the required experimental pressure. The reactor was then heated to the required temperature (120–180 °C) upon stirring at 550 rpm. After the desired reaction time (1–8 h), the reactor was rapidly quenched in a cold-water bath. Once the temperature reached 25

± 2 °C, the reactor was depressurized to atmospheric pressure. Then, the reaction mixture was collected and separated from the catalyst by centrifugation. Prior to quantification, 1 µL/mL dodecane was added to the reaction mixture as an internal standard.

The reaction products were qualitatively analyzed using gas chromatography–time-of-flight mass spectrometry (GC-TOF/MS). An Agilent 7890 N GC (Agilent Technologies, USA) coupled to a Pegasus high-throughput TOF/MS system (Leco Corporation, USA) was equipped with an autoinjector (Agilent 7860 N) and a middle-range polarity column (Rxi-5Sil-MS, Restek; 30 m × 0.25 µm × 0.25 mm ID). Ultrahigh-purity He (99.9999%) was used as the carrier gas. Typically, 1 µL of the liquid product was injected into the GC column at a split ratio of 25:1. The injector and transfer line temperatures were set at 250 and 260 °C, respectively. The column temperature program was initially held at 40 °C for 2 min and then increased to 250 °C at a rate of 10 °C min⁻¹. Quantitative analysis was performed using an Agilent 6890 N GC instrument (Agilent Technologies, USA) equipped with a capillary column (Rxi-5Sil-MS, Restek; 30 m × 0.25 µm × 0.25 mm ID) and a flame ionization detector (FID). Typically, 1 µL of the reaction product was injected into the GC column at a split ratio of 1:10. The inlet and detector temperatures were both set at 250 °C. The column temperature was initially held at 50 °C for 2 min and then increased to 250 °C at a rate of 10 °C min⁻¹ and held for 5 min before cooling to 50 °C. The yields and selectivities of the intermediates and products were determined by calibrating the column with corresponding standards. The FFA conversion, product selectivity, and product yield, were calculated from the GC-FID results using the following equations.

$$\text{Conversion(\%)} = \left(1 - \frac{\text{moles of unreacted FFA}}{\text{moles of initial FFA}} \right) \times 100 \quad (1)$$

$$\text{Yield(\%)} = \frac{\text{moles of product A}}{\text{moles of initial FFA}} \times 100 \quad (2)$$

$$\text{Selectivity(\%)} = \frac{\text{moles of product A}}{\text{moles of reacted FFA}} \times 100 \quad (3)$$

2.5. Computational method

The CASTEP program in the Materials Studio 2022 package was employed for spin-polarized DFT calculations. For the exchange correlation energies of electrons, the generalized gradient approximation (GGA) method was applied with the Perdew–Burke–Ernzerhof (PBE) functional [34]. Plane-wave basis sets were employed with a cutoff energy of 400 eV [35]. The interactions between ion cores and valence electrons were computed using the projector augmented-wave method. Geometry optimization and energy calculations employed convergence tolerances of 2×10^{-6} eV atom⁻¹, 2×10^{-5} eV atom⁻¹, 0.05 eV Å⁻¹, and 0.002 Å for the self-consistent field, energy, maximum force, and maximum displacement, respectively [36,37].

Catalyst model slabs comprising four layers were constructed using 4×4 unit cells of Ni (111), 2×1 unit cells of Co₃O₄ (110), and 2×1 unit cells of O_v–Co₃O₄ (110). The bottom two layers were constrained to prevent atom displacement during optimization calculations, whereas relaxation of the top two layers was allowed to achieve the optimized configuration. This relaxation process was used to account for surface restoration. A vacuum slab with a thickness of 20 Å was introduced between the topmost layer of the slab and the bottom layer of the next slab to minimize interactions between slabs. The Brillouin zone was sampled with a $2 \times 2 \times 1$ k-point grid. For calculations of Co₃O₄ (110) and O_v–Co₃O₄ (110), surface magnetism via spin polarization was considered to impart Co₃O₄ with the type-II antiferromagnetic character [38,39]. CoO unit cell simulations were not performed because the surface was unstable, even when employing the U parameter. The U parameter here is the effective Hubbard U parameter (U_{eff}), and the value of 3.40 eV was adopted for 3d orbital of Co in Co₃O₄ (110).

Adsorbates were introduced on the top layer of the slab. Geometry optimization calculations were performed to yield the relaxed adsorbate structures on the Ni (111), Co_3O_4 (110), and oxygen-vacant Co_3O_4 (110) slabs. The adsorption energy of an adsorbate (E_{ads}) was calculated using Eq. 4:

$$E_{\text{ads}} = E_{\text{slab+adsorbate}} - E_{\text{slab}} - E_{\text{adsorbate}} \quad (4)$$

where $E_{\text{slab+adsorbate}}$ is the overall energy of the adsorbate on the catalyst slab, E_{slab} is the energy of the clean slab, and $E_{\text{adsorbate}}$ is the energy of the free adsorbate in the gas phase.

Reaction coordinate calculations were performed using the synchronous transit method, which uses a linear model to optimize reactants, intermediates, and final products with the same relative position along the path [40]. Transition states with one imaginary frequency were calculated using vibrational frequency analysis. In addition, the nudged elastic band method was used to calculate the intrinsic reaction coordinate, so that each transition state was connected with the corresponding reactants and products [41,42]. All transition-state calculations were performed at the same level of theory as the geometry optimization and energy calculations.

For each reaction step, the activation energy (ΔE_A) and reaction energy (ΔE_r) were calculated using Eqs. 5 and 6, respectively:

$$\Delta E_A = E_{\text{TS}} - E_{\text{IS}} \quad (5)$$

$$\Delta E_r = E_{\text{FS}} - E_{\text{IS}} \quad (6)$$

where E_{IS} , E_{TS} , and E_{FS} are the energies of the reactant, transition state, and product, respectively.

3. Results and discussion

3.1. Catalyst characterization

The phase structure and crystallinity of the catalysts were examined by XRD analysis (Fig. 2a). The $\text{Ni}_8\text{Al}_1(1:2)\text{-OR}$ catalyst exhibits broad peaks at $2\theta = 37.4^\circ$, 43.3° , and 63.1° , assigned to the (111), (200), and (220) planes of NiO (PDF#01-1278), and relatively intense peaks at $2\theta = 44.5^\circ$ and 51.9° , assigned to the (111) and (200) planes of Ni^0 (PDF#04-0850), respectively. Despite a high alumina loading (13.3 wt %, Table 1), the $\text{Ni}_8\text{Al}_1(1:2)\text{-OR}$ catalyst exhibits no peaks associated with alumina, indicating its amorphous nature. In the case of the $\text{Co}_8\text{Al}_1(1:2)\text{-OR}$ catalyst, the peaks at 36.3° , 42.4° , and 62.1° are assigned to the (111), (200), and (220) planes of CoO (PDF#46-1719), respectively. The slight shift of these peaks toward larger angles is attributed to Al dissolution in the tetrahedral Co^{2+} site [43]. The preferential insertion of Al^{3+} into the Co sites as compare to the Ni sites is because the enthalpy of formation of CoAl_2O_4 spinel is lower ($\Delta H_{970\text{K}} = -37.2 \text{ kJ mol}^{-1}$) than that of NiAl_2O_4 spinel ($\Delta H_{970\text{K}} = -3.1 \text{ kJ mol}^{-1}$) [44]. During the reduction of Co^{3+} to Co^0 in the Co_3O_4 nanoparticles (NPs) synthesized using the coprecipitation method at 450°C [45], Al^{3+} dissolution in the Co oxide phase and a strong interaction between the Co oxide and alumina phases suppressed the formation of a metallic Co^0 phase in the $\text{Co}_8\text{Al}_1(1:2)\text{-OR}$ catalyst. The $\text{Ni}_4.5\text{Co}_{3.5}(1:2)\text{-OR}$ catalyst exhibits intense peaks at $2\theta = 44.5^\circ$, 51.6° , and 76.1° , corresponding to the (111), (200), and (220) planes of Ni^0 (PDF#04-0850), respectively. The slight shift of these peaks toward smaller angles is attributed to the formation of a Ni-Co alloy [46]. The trimetallic $\text{Ni}_{4.5}\text{Co}_{3.5}\text{Al}_1(1:0)\text{-OR}$ catalyst exhibits relatively intense NiO peaks and weak Ni^0 peaks. By contrast, the $\text{Ni}_{4.5}\text{Co}_{3.5}\text{Al}_1(1:2)\text{-OR}$ and $\text{Ni}_{4.5}\text{Co}_{3.5}\text{Al}_1(1:2)\text{-R}$ catalysts exhibit weak, broad NiO peaks and no Ni^0 peaks are observed. Thus, NiO crystal

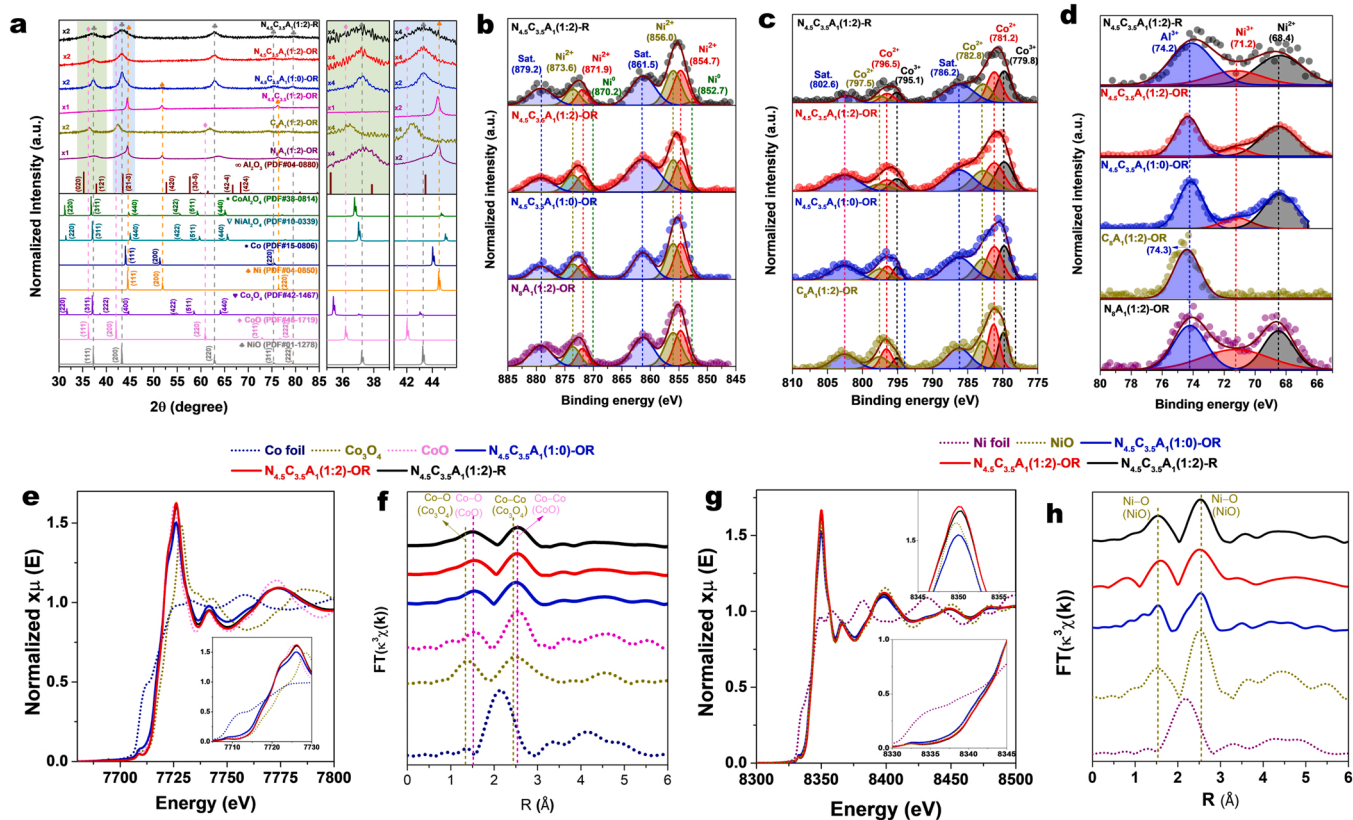


Fig. 2. (a) XRD patterns; (b) Ni 2p, (c) Co 2p, and (d), Al 2p XPS core-level spectra; (e) normalized Co K-edge XANES spectra; (f) k^3 -weighted Fourier transforms of normalized Co K-edge EXAFS spectra ($k^3\chi(k)$); (g) normalized Ni K-edge XANES spectra; and (h) k^3 -weighted Fourier transforms of normalized Ni K-edge EXAFS spectra ($k^3\chi(k)$) of bimetallic and trimetallic catalysts.

Table 1

Properties of bimetallic and trimetallic catalysts.

Catalyst	Ni/Co/Al loading (wt%) ^a	Ni ⁰ /NiO/CoO crystallite size (d ₁₁₁) (nm) ^b	S _{BET} ^c (m ² g ⁻¹)	S _{micro} ^d (m ² g ⁻¹)	V _{micro} ^e (cm ³ g ⁻¹)	V _{meso} ^f (cm ³ g ⁻¹)	V _{total} ^g (cm ³ g ⁻¹)	Mean pore diameter ^h (nm)
N ₈ A ₁ -OR(1:2)-OR	86.7/0/13.3	4.59/3.50/-	169.6	165.88	0.294	0.012	0.306	7.1
C ₈ A ₁ -OR(1:2)-OR	0/85.8/14.2	-/-/5.47	95.9	0	0	0.652	0.652	27.4
N _{4.5} C _{3.5} A ₁ (1:2)-OR	52.8/47.2/0	22.2/-/-	27.5	0	0	0.212	0.212	31.1
N _{4.5} C _{3.5} A ₁ (1:0)-OR	45.5/40.7/13.7	-/5.21/-	57.3	50.89	0.176	0.013	0.189	12.9
N _{4.5} C _{3.5} A ₁ (1:2)-OR	45.6/40.9/13.5	-/3.92/-	166.0	90.7	0.387	0.171	0.521	12.5
N _{4.5} C _{3.5} A ₁ (1:2)-R	49.3/39.6/11.1	-/3.23/-	182.9	94.9	0.314	0.154	0.468	10.6
N _{4.5} C _{3.5} A ₁ (1:2)-R-S ⁱ	49.2/39.5/11.3	-/2.18/-	202.3	54.5	0.173	0.106	0.279	9.9

^a Measured using ICP-OES.^b Determined from the Ni⁰ (111), NiO (111), and CoO (111) planes using the Scherrer equation.^c BET specific surface area.^d Micropore surface area determined by the t-plot method.^e Micropore volume determined by the t-plot method.^f Micropore volume determined by the BJH method.^g Total volume adsorbed at P/P₀ = 0.99.^h Mean pore diameter determined by the BET method.ⁱ Spent catalyst collected after four consecutive runs.^j Determined from the NiO (200) plane using the Scherrer equation.

growth was suppressed by using NaOH and Na₂CO₃ as coprecipitants. The crystallite sizes of Ni⁰, NiO, and CoO estimated from the corresponding (111) planes using the Scherrer equation are listed in Table 1. Notably, the N_{4.5}C_{3.5}A₁(1:2)-OR and N_{4.5}C_{3.5}A₁(1:2)-R catalysts have smaller NiO crystallite sizes than the N_{4.5}C_{3.5}A₁(1:0)-OR catalyst.

The chemical environments of the catalysts were investigated through XPS (Fig. 2b–d). In the Ni 2p XPS profiles of the bimetallic and trimetallic catalysts, the peaks at 852.7 and 870.2 eV are associated with metallic Ni⁰ 2p_{3/2} and 2p_{1/2}, respectively [40]. The peaks at 854.7 and 871.9 eV are assigned to Ni²⁺ (NiO), whereas the peaks at 856.0 and 873.6 eV are attributed to Ni²⁺ ions surrounded by Al³⁺ ions with O²⁻ interconnections [47]. In the case of the N_{4.5}C_{3.5}A₁(1:0)-OR catalyst, the preferential growth of the Ni⁰ phase resulted in Ni⁰ being exposed near the surface. However, the use of NaOH and Na₂CO₃ as coprecipitants in the trimetallic catalysts effectively suppressed Ni⁰ formation at the surface (Table S2). In the Co 2p XPS profiles, the peaks at 779.8 and 795.1 eV are assigned to Co³⁺ (Co₃O₄) 2p_{3/2} and 2p_{1/2}, respectively, the peaks at 781.2 and 796.5 eV are assigned to Co²⁺ (CoO) 2p_{3/2} and 2p_{1/2}, respectively, and the peaks at 782.8 and 797.5 eV are assigned to Co²⁺ (Co₃O₄) 2p_{3/2} and 2p_{1/2}, respectively, or Co²⁺ ions surrounded by Al³⁺ ions with O²⁻ interconnections [48]. Considering the almost negligible XRD peaks of CoO and Co₃O₄, the presence of Co³⁺ and Co²⁺ peaks in the XPS profiles indicates that the trimetallic catalysts contain highly dispersed, ultrasmall Co oxide domains. The Al 2p XPS profiles exhibit a peak at 74.2 eV, assigned to Al³⁺ (Al₂O₃) [49]. The presence of alumina peaks in the XPS profiles combined with the absence of alumina peaks in the XRD patterns can be attributed to the amorphous nature of this component in the bimetallic and trimetallic catalysts.

The oxidation states and local chemical structures of Ni and Co in the trimetallic catalysts were analyzed through XAS. In the Co K-edge XANES spectrum of the N_{4.5}C_{3.5}A₁(1:0)-OR catalyst (Fig. 2e), the onset of the absorption edge is shifted toward lower energies and the height of the white line peak is decreased relative to those in the spectra of the N_{4.5}C_{3.5}A₁(1:2)-OR and N_{4.5}C_{3.5}A₁(1:2)-R catalysts. Comparison with the CoO and Co₃O₄ standard profiles indicates that Co⁰, Co²⁺, and Co³⁺ coexist in the N_{4.5}C_{3.5}A₁(1:0)-OR catalyst, whereas Co²⁺ and Co³⁺ coexist in the N_{4.5}C_{3.5}A₁(1:2)-OR and N_{4.5}C_{3.5}A₁(1:2)-R catalysts. The k³-weighted Fourier-transform magnitudes of the Co K-edge EXAFS spectra of the trimetallic catalysts and corresponding references reveal the presence of a Co–Co scattering path at 2.55 Å, confirming the presence of CoO (Fig. 2f). The EXAFS profiles were fitted to extract the coordination numbers (CNs) of Co (Fig. S2 and Table S3). The CN of Co–O in the CoO phase of the N_{4.5}C_{3.5}A₁(1:0)-OR catalyst (4.1) is smaller than those of the N_{4.5}C_{3.5}A₁(1:2)-OR (5.1) and N_{4.5}C_{3.5}A₁(1:2)-R catalysts (4.4). In addition, the CNs of Co–O in the Co₃O₄ phase of the

N_{4.5}C_{3.5}A₁(1:0)-OR and N_{4.5}C_{3.5}A₁(1:2)-OR catalysts (1.0) are larger than that of the N_{4.5}C_{3.5}A₁(1:2)-R catalyst (0.8). Thus, directly reducing the coprecipitated precursors without an additional calcination step resulted in more unsaturated sites in the Co₃O₄ domain and thus a high content of O_v sites. In the Ni K-edge XANES spectrum of the N_{4.5}C_{3.5}A₁(1:0)-OR catalyst, the onset of the absorption edge is shifted toward lower energies and the height of the white line peak is decreased relative to those in the spectra of the N_{4.5}C_{3.5}A₁(1:2)-OR and N_{4.5}C_{3.5}A₁(1:2)-R catalysts. The Ni oxidation states in the N_{4.5}C_{3.5}A₁(1:2)-R, N_{4.5}C_{3.5}A₁(1:2)-OR, and N_{4.5}C_{3.5}A₁(1:0)-OR catalysts were slightly lower than that in the Ni⁽²⁺⁾O standard. The k³-weighted Fourier-transform magnitudes of the Ni K-edge EXAFS spectra reveal Ni–O scattering paths at 1.53 and 2.53 Å, indicating that the major Ni oxidation state in the catalysts was Ni⁽²⁺⁾O. The CN of metallic Ni–Ni bonds in the N_{4.5}C_{3.5}A₁(1:0)-OR catalyst (1.6) is larger than those of the N_{4.5}C_{3.5}A₁(1:2)-OR (0.7) and N_{4.5}C_{3.5}A₁(1:2)-R catalysts (1.0), indicating that the use of NaOH and Na₂CO₃ as coprecipitants resulted in smaller Ni⁰ nanoclusters than the use of NaOH alone (Table S3 and Fig. S3) [50]. According to the linear combination fitting results, the metallic Ni⁰ contents in the trimetallic catalysts decrease in the order of N_{4.5}C_{3.5}A₁(1:0)-OR (14.5%) >> N_{4.5}C_{3.5}A₁(1:2)-R (3.2%) > N_{4.5}C_{3.5}A₁(1:2)-OR (1.4%) (Table S4). Overall, the N_{4.5}C_{3.5}A₁(1:2)-OR and N_{4.5}C_{3.5}A₁(1:2)-R catalysts contain extremely small Ni⁰ nanoclusters, O_v sites in the Co oxide phases, and bulk CoO and NiO phases, whereas the N_{4.5}C_{3.5}A₁(1:0)-OR has discrete metallic Ni⁰ phases.

The morphologies and textural properties of the catalysts were examined through HR-TEM and N₂ adsorption–desorption isotherms. The N₈A₁(1:2)-OR catalyst has a particle size of 2–10 nm (average: 5 nm, Figs. S4a and b). High-resolution STEM and fast Fourier transform (FFT) images reveal the presence of the (311) and (111) planes of Ni⁰ and the (202) plane of NiO (Figs. S4c and d). Similarly, the C₈A₁(1:2)-OR catalyst exhibits fine particles with sizes of 3–10 nm (Figs. S4e and f), and both CoO and Co₃O₄ phases are observed in high-resolution STEM and FFT images (Figs. S4g and h). By contrast, a high degree of particle aggregation with sizes of 25–300 nm occurs in the N_{4.5}C_{3.5}(1:2)-OR catalyst (Figs. S4i and j). The presence of metallic Ni⁰ and Co⁰ and the corresponding oxides phases (NiO and Co₃O₄) is revealed by STEM and FFT images (Figs. S4k and l). The N₂ adsorption–desorption isotherms of all the catalysts exhibit type IV behavior with an H1 hysteresis loop, indicating the presence of mesoporous structures (Fig. S5). The BET surface area of the N_{4.5}C_{3.5}(1:2)-OR catalyst (27.5 m² g⁻¹) is much smaller than those of the C₈A₁(1:2)-OR and N₈A₁(1:2)-OR catalysts (95.9 and 169.9 m² g⁻¹, respectively, Table 1). Thus, the presence of alumina suppressed particle growth during calcination and reduction.

The $\text{N}_{4.5}\text{C}_{3.5}\text{A}_1(1:0)\text{-OR}$ catalyst contains spherical particles with sizes of 6–30 nm (average: 14 nm, Fig. 3a), whereas mixed needle-like and spherical particles are present in the $\text{N}_{4.5}\text{C}_{3.5}\text{A}_1(1:2)\text{-OR}$ and $\text{N}_{4.5}\text{C}_{3.5}\text{A}_1(1:2)\text{-R}$ catalysts with average particle sizes of 4.2 and 4.9 nm, respectively (Fig. 3i and q). The BET surface area of the $\text{N}_{4.5}\text{C}_{3.5}\text{A}_1(1:0)\text{-OR}$ catalyst ($57.3 \text{ m}^2 \text{ g}^{-1}$) is lower than those of the $\text{N}_{4.5}\text{C}_{3.5}\text{A}_1(1:2)\text{-OR}$ and $\text{N}_{4.5}\text{C}_{3.5}\text{A}_1(1:2)\text{-R}$ catalysts (166.0 and $182.9 \text{ m}^2 \text{ g}^{-1}$, respectively, Table 1). Thus, the use of NaOH and Na_2CO_3 as coprecipitates effectively suppressed particle growth. The STEM image of the $\text{N}_{4.5}\text{C}_{3.5}\text{A}_1(1:0)\text{-OR}$ catalyst shows d-spacings of 0.136, 0.148, 0.205, and 0.285 nm, which correspond to the (513) plane of Co_3O_4 , (202) plane of NiO , (111) plane of Ni , and (110) plane of Co_3O_4 , respectively (Fig. 3b and c). The $\text{N}_{4.5}\text{C}_{3.5}\text{A}_1(1:2)\text{-OR}$ and $\text{N}_{4.5}\text{C}_{3.5}\text{A}_1(1:2)\text{-R}$ catalysts exhibit d-spacings of 0.205 and 0.285 nm, which are assigned to the (111) plane of Ni^0 and (110) plane of Co_3O_4 , respectively (Fig. 3j, k, r, and s). Further inspection of the trimetallic $\text{N}_{4.5}\text{C}_{3.5}\text{A}_1(1:2)\text{-OR}$ and $\text{N}_{4.5}\text{C}_{3.5}\text{A}_1(1:2)\text{-R}$ catalysts reveals that the Co_3O_4 and Ni phases are in close proximity. The high-angle annular dark field (HAADF)-STEM images and corresponding EDS mapping of the trimetallic catalysts indicate that Ni , Co , and Al are uniformly distributed throughout the catalysts (Fig. 3d–h, l–p, and t–x).

Catalyst reducibility was determined through H_2 -TPR analysis (Fig. 4a and Table S5). The $\text{N}_8\text{A}_1(1:2)\text{-OR}$ catalyst exhibits weak, broad peaks at 396 and 420 °C, attributed to the reduction of isolated NiO to Ni^0 [51], and intense peaks at 671 and 733 °C, attributed to the reduction of Ni^{2+} species in the Ni -rich and Ni -lean phases, respectively, of a defective $\text{Ni}_{1-x}\text{Al}_2\text{O}_{4-x}$ structure [52,53]. For the $\text{C}_8\text{A}_1(1:2)\text{-OR}$ catalyst, the peaks at low-to-medium temperatures of 429 and 447 °C are assigned to the reduction of Co_3O_4 to CoO and the subsequent reduction of CoO to Co^0 , whereas the high-temperature peaks at 670–780 °C are attributed to the reduction of Co^{2+} in a defective $\text{Co}_{1-x}\text{Al}_2\text{O}_{4-x}$ structure [54]. The $\text{N}_{4.5}\text{C}_{3.5}(1:2)\text{-OR}$ catalyst without Al species shows multistep reduction processes at temperatures of 260–515 °C. Overlapping reduction temperatures for Co and Ni oxide species complicate the assignment of individual desorption peaks. Nevertheless, the low-temperature peaks at 260–370 °C can be attributed to exposed $\text{Co}_3\text{O}_4 \rightarrow \text{CoO} \rightarrow \text{Co}^0$, whereas the high-temperature peaks at 480–515 °C can be assigned to $\text{NiO} \rightarrow \text{Ni}^0$ [51,55]. Although the trimetallic $\text{Ni-CoO}_x\text{-Al}_2\text{O}_3$ catalysts exhibit bimodal desorption profiles similar to those of the bimetallic catalysts, the reduction temperatures in the low-temperature regime are lower, suggesting the presence of exposed NiO and Co_3O_4 species. The exposed $\text{Co}_3\text{O}_4 \rightarrow \text{CoO} \rightarrow \text{Co}^0$ and $\text{NiO} \rightarrow \text{Ni}^0$ peaks of the $\text{N}_{4.5}\text{C}_{3.5}\text{A}_1(1:2)\text{-OR}$ and $\text{N}_{4.5}\text{C}_{3.5}\text{A}_1(1:2)\text{-R}$ catalysts are located at lower temperatures than those of the $\text{N}_{4.5}\text{C}_{3.5}\text{A}_1(1:0)\text{-OR}$ catalyst, which can be attributed to the presence of much smaller particles (Fig. 3). Unlike the $\text{N}_{4.5}\text{C}_{3.5}\text{A}_1(1:2)\text{-OR}$ and $\text{N}_{4.5}\text{C}_{3.5}\text{A}_1(1:2)\text{-R}$ catalysts, the $\text{N}_{4.5}\text{C}_{3.5}\text{A}_1(1:0)\text{-OR}$ catalyst exhibits an additional peak at 573 °C, which implies the presence of discrete Co and Ni oxides that strongly interact with the Al species. Thus, the ultrasmall Co and Ni oxide NPs, formed when using NaOH and Na_2CO_3 as coprecipitants, were incorporated into the defective $\text{Ni}_{1-x}\text{Al}_2\text{O}_{4-x}$ and $\text{Co}_{1-x}\text{Al}_2\text{O}_{4-x}$ spinel structures in the $\text{N}_{4.5}\text{C}_{3.5}\text{A}_1(1:2)\text{-OR}$ and $\text{N}_{4.5}\text{C}_{3.5}\text{A}_1(1:2)\text{-R}$ catalysts.

To examine the O_v sites on the catalyst surfaces, O_2 -TPD profiles were collected (Fig. 4b and Table S6). The oxygen species on the metal oxide surfaces can be categorized into physically adsorbed oxygen ($\text{O}_{2(\text{ads})}$) below 100 °C, superoxide species ($\text{O}_{2(\text{ads})}^-$) at 100–200 °C, monatomic oxygen ($\text{O}_{(\text{ads})}$) at 200–400 °C, surface lattice oxygen ($\text{O}_{\text{latt}(\text{surface})}^2$) at 400–700 °C, and bulk lattice oxygen ($\text{O}_{\text{latt}(\text{bulk})}^2$) above 700 °C [56–58]. The $\text{N}_8\text{A}_1(1:2)\text{-OR}$ catalyst only exhibits an O_2 desorption peak at 850 °C, indicating the absence of surface O_v sites. In the Co_3O_4 NPs synthesized using the coprecipitation method, the main desorbed species is $\text{O}_{\text{latt}(\text{bulk})}^2$ ($2.603 \text{ mmol g}_{\text{Co}}^{-1}$). However, the presence of Al species prevented the formation of $\text{O}_{\text{latt}(\text{bulk})}^2$ in the $\text{C}_8\text{A}_1(1:2)\text{-OR}$ catalyst ($0.057 \text{ mmol g}_{\text{Co}}^{-1}$). The formation of Co-O-Al bonds in the spinel $\text{Co}_{1-x}\text{Al}_2\text{O}_{4-x}$ structure suppressed $\text{O}_{\text{latt}(\text{bulk})}^2$ desorption, likely because the bonding energy of Al-O

(511 kJ mol^{-1}) is higher than that of Co-O (368 kJ mol^{-1}) [59]. The metallic nature of the Co and Ni species in the $\text{N}_{4.5}\text{C}_{3.5}(1:2)\text{-OR}$ catalyst resulted in negligible O_2 desorption. The $\text{N}_{4.5}\text{C}_{3.5}\text{A}_1(1:0)\text{-OR}$ catalyst exhibits desorption peaks associated with $\text{O}_{2(\text{ads})}^-$, $\text{O}_{(\text{ads})}^-$, and $\text{O}_{\text{latt}(\text{surface})}^2$, whereas the main desorbed species for the $\text{N}_{4.5}\text{C}_{3.5}\text{A}_1(1:2)\text{-OR}$ and $\text{N}_{4.5}\text{C}_{3.5}\text{A}_1(1:2)\text{-R}$ catalysts are $\text{O}_{\text{latt}(\text{surface})}^2$ and $\text{O}_{\text{latt}(\text{bulk})}^2$. Thus, close proximity between CoO_x and alumina phases as well as embedding ultrasmall CoO_x domains in the defective $\text{Co}_{1-x}\text{Al}_2\text{O}_{4-x}$ spinel structure suppressed the low-temperature desorption of oxygen. Based on the Co contents of the catalysts, the oxygen amounts desorbed from the surface lattice region decrease in the order of $\text{N}_{4.5}\text{C}_{3.5}\text{A}_1(1:2)\text{-R}$ ($0.399 \text{ mmol g}_{\text{Co}}^{-1}$) $>$ $\text{N}_{4.5}\text{C}_{3.5}\text{A}_1(1:2)\text{-OR}$ ($0.251 \text{ mmol g}_{\text{Co}}^{-1}$) $>$ $\text{C}_8\text{A}_1(1:2)\text{-OR}$ ($0.241 \text{ mmol g}_{\text{Co}}^{-1}$) $>$ $\text{N}_{4.5}\text{C}_{3.5}\text{A}_1(1:0)\text{-OR}$ ($0.221 \text{ mmol g}_{\text{Co}}^{-1}$) $>$ Co_3O_4 ($0.151 \text{ mmol g}_{\text{Co}}^{-1}$). Therefore, the omission of the additional calcination step during catalyst synthesis facilitated the formation of surface lattice oxygen vacancies ($\text{O}_v\text{-CoO}_x$) in the trimetallic $\text{N}_{4.5}\text{C}_{3.5}\text{A}_1(1:2)\text{-R}$ catalyst. The presence of O_v sites aids in creating unsaturated metal centers ($\text{Co}^{\delta+}$), which are active for FFA adsorption through electron donation to the C=O bond [60].

H_2 -TPD analysis was performed to examine the dissociative adsorption of H_2 on the catalyst surfaces (Fig. 4c and Table S7). During TPD analysis, the desorbed species were monitored using QMS, and the H_2 desorption profiles were adjusted using the primary mass profile of $m/z = 2$ (Fig. S6). H_2 desorption can be divided into two regions: low-to-medium temperature desorption (<400 °C), corresponding to hydrogen dissociated and chemisorbed on metallic sites and hydrogen at the interface between metal NPs and the metal oxide surface, and high-temperature desorption (>400 °C), attributable to hydrogen in the subsurface region and spillover hydrogen [61,62]. The $\text{N}_8\text{A}_1(1:2)\text{-OR}$ catalyst exhibits peaks corresponding to both dissociated hydrogen on the Ni^0 surface and spillover hydrogen. However, because of the absence of exposed metallic Co^0 sites, the $\text{C}_8\text{A}_1(1:2)\text{-OR}$ catalyst only exhibits a high-temperature desorption peak centered at 680 °C, which indicates that dissociative H_2 adsorption is only feasible on the surface of Co oxides. By contrast, the $\text{N}_{4.5}\text{C}_{3.5}(1:2)\text{-OR}$ catalyst exhibits low-temperature desorption peaks at 106 and 166 °C, which are attributed to dissociative H_2 adsorption on exposed Ni^0 and Co^0 sites. Because the $\text{N}_{4.5}\text{C}_{2.5}\text{A}_1(1:0)\text{-OR}$ catalyst is richer in metallic Ni^0 sites, H_2 desorption occurs at a low temperature of 299 °C, whereas the Ni^0 -deficient $\text{N}_{4.5}\text{C}_{2.5}\text{A}_1(1:2)\text{-OR}$ and $\text{N}_{4.5}\text{C}_{2.5}\text{A}_1(1:2)\text{-R}$ catalysts exhibit no low-temperature desorption peaks. The high-temperature peaks at 420–558 °C for the trimetallic catalysts indicate the presence of spillover hydrogen in the $\text{O}_v\text{-Co}_x\text{O}_y$, Co_3O_4 , and spinel phases. The small metallic Ni^0 domains in the $\text{N}_{4.5}\text{C}_{2.5}\text{A}_1(1:2)\text{-OR}$ and $\text{N}_{4.5}\text{C}_{2.5}\text{A}_1(1:2)\text{-R}$ catalysts facilitated dissociative H_2 adsorption in relation to those in the $\text{C}_8\text{A}_1(1:2)\text{-OR}$ catalyst. The amount of spillover hydrogen decreases in the order of $\text{N}_{4.5}\text{C}_{2.5}\text{A}_1(1:2)\text{-R}$ ($0.313 \text{ mmol g}^{-1}$) $>$ $\text{N}_{4.5}\text{C}_{2.5}\text{A}_1(1:2)\text{-OR}$ ($0.237 \text{ mmol g}^{-1}$) $>$ $\text{N}_{4.5}\text{C}_{3.5}\text{A}_1(1:0)\text{-OR}$ ($0.216 \text{ mmol g}^{-1}$). Thus, the presence of metallic Ni^0 sites and enrichment of surface O_v sites in the CoO_x phase facilitated the formation of spillover hydrogen on the $\text{N}_{4.5}\text{C}_{2.5}\text{A}_1(1:2)\text{-R}$ catalyst (Fig. S7).

To understand the acidic properties of the catalysts, pyridine-DRIFT and NH_3 -TPD profiles were collected. In the pyridine-DRIFT profiles (Fig. 5a), the bands at 1448 and 1607 cm^{-1} correspond to pyridine adsorption on Lewis acid sites (LASs, e.g., metal centers, Ni^{2+} , Co^{2+} , and Al^{3+}) and the bands at 1435, 1487, and 1584 cm^{-1} originate from hydrogen-bonded pyridine molecules on the metal oxide surface (e.g., $\text{Ni}(\text{OH})_2$) [63]. The NH_3 -TPD profiles (Fig. 5b and Table S8), which were corrected using the secondary mass profile of $m/z = 16$ (Fig. S8), can be divided into three regions: weak (<250 °C), medium (250–400 °C), and strong (>400 °C) acid sites. Weak acidity is attributed to the desorption of weakly adsorbed NH_3 on the weak LASs of the metal centers, medium acidity originates from the interaction of NH_3 with the Al^{3+} sites of Al_2O_3 and $\text{M}_{1-x}\text{Al}_2\text{O}_{4-x}$ ($\text{M} = \text{Co}, \text{Ni}$), and strong acidity is ascribed to NH_3 coordination with electron-deficient metal oxides (e.g., $\text{O}_v\text{-CoO}_x$) [64,65]. The bimetallic $\text{N}_8\text{A}_1(1:2)\text{-OR}$ and $\text{C}_8\text{A}_1(1:2)\text{-OR}$ catalysts exhibit weak, broad peaks in the weak-to-medium region with low total

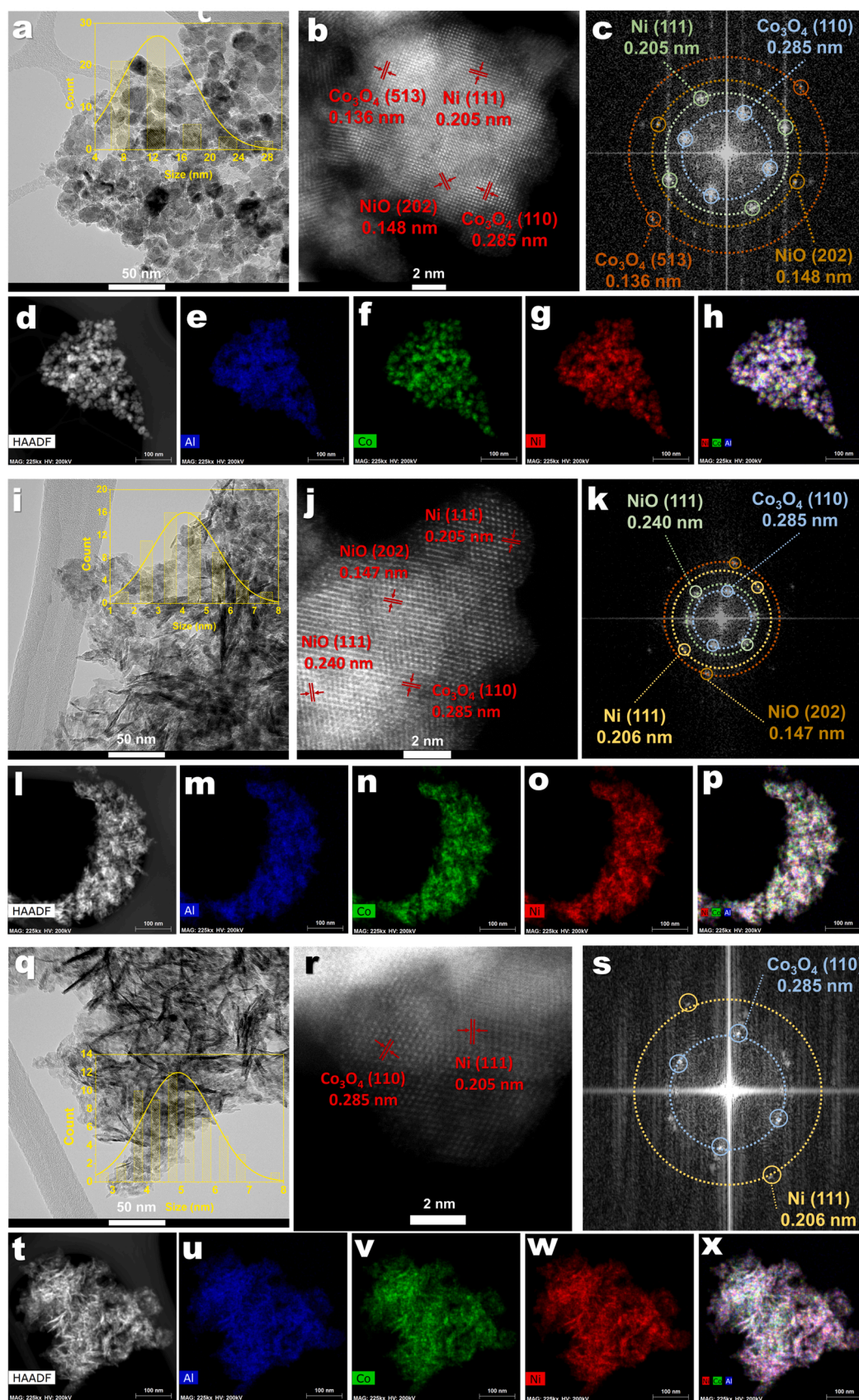


Fig. 3. (a) and (b) HR-TEM images, (c) FFT image, and (d–h) HAADF-STEM image with corresponding EDS mapping of Al, Co, and Ni for $N_{4.5}C_{3.5}A_1(1:0)$ -OR. (i) and (j) HR-TEM images, (k) FFT image, and (l–p) HAADF-STEM image with corresponding EDS mapping of Al, Co, and Ni for $N_{4.5}C_{3.5}A_1(1:2)$ -OR. (q) and (r) HR-TEM images, (s) FFT image, and (t–x) HAADF-STEM image with corresponding EDS mapping of Al, Co, and Ni for $N_{4.5}C_{3.5}A_1(1:2)$ -R.

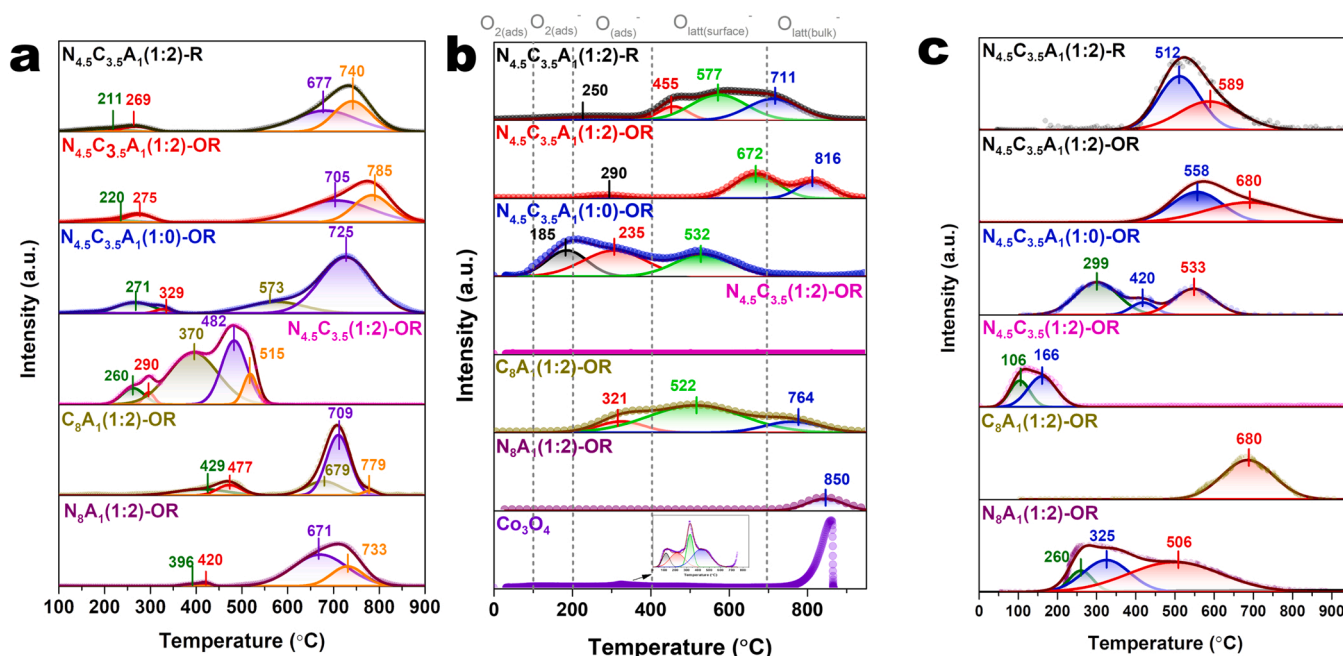


Fig. 4. (a) H_2 -TPR, (b) O_2 -TPD, and (c) H_2 -TPD profiles of bimetallic and trimetallic catalysts.

acidities of 0.21–0.27 mmol g^{-1} . By contrast, the trimetallic $\text{N}_{4.5}\text{C}_{3.5}\text{A}_1(1:0)\text{-OR}$, $\text{N}_{4.5}\text{C}_{3.5}\text{A}_1(1:2)\text{-OR}$, and $\text{N}_{4.5}\text{C}_{3.5}\text{A}_1(1:2)\text{-R}$ catalysts exhibit intense peaks with high total acidities of 0.43–0.52 mmol g^{-1} . Thus, more metal centers (Ni^{2+} , Co^{2+} , and Al^{3+}) were exposed on the surfaces of the trimetallic catalysts, which can be attributed to the suppression of metallic Ni^0 phase formation. Consequently, the majority of the metal centers in the trimetallic catalysts could act as LASSs. The negligible adsorption of NH_3 on the $\text{N}_{4.5}\text{C}_{3.5}(1:2)\text{-OR}$ catalyst is due to the predominance of metallic Ni^0 and Co^0 sites on the surface. The $\text{N}_{4.5}\text{C}_{3.5}\text{A}_1(1:2)\text{-R}$ catalyst exhibits a high-temperature peak centered at 486 $^\circ\text{C}$, which is attributed to NH_3 adsorption on coordinated unsaturated metal centers (Co^{2+}) adjacent to O_v sites [64].

To investigate the surface atomic arrangement and electronic properties of the Ni and Co species on the catalyst surfaces, CO-DRIFT profiles were collected during CO adsorption and desorption (Fig. S9). To avoid interference from the IR bands of gaseous CO, the CO-DRIFT profiles were collected after flushing with N_2 for 20 min (Fig. 5c). The $\text{N}_8\text{A}_1(1:2)\text{-OR}$ catalyst exhibits small peaks centered at 2012 and 1993 cm^{-1} , which are assigned to two-fold bridged CO on different crystal planes of the Ni NPs [66,67]. The broad peaks centered at 1880 and 1850 cm^{-1} are assigned to three-fold bridged CO on the terrace regions of face-centered cubic (fcc) and hexagonal close-packed (hcp) hollow sites of Ni^0 , respectively [68]. No CO species were adsorbed on the $\text{C}_8\text{A}_1(1:2)\text{-OR}$ catalyst because of the absence of metallic sites [69]. The $\text{Ni}_{4.5}\text{C}_{3.5}(1:2)\text{-OR}$ catalyst exhibits peaks at 2078 and 2061 cm^{-1} , which correspond to multicoordinated CO and linearly adsorbed CO on individual Ni^0 sites, respectively [67]. By contrast, no linearly adsorbed CO was observed on the $\text{N}_{4.5}\text{C}_{3.5}\text{A}_1(1:2)\text{-OR}$ and $\text{N}_{4.5}\text{C}_{3.5}\text{A}_1(1:2)\text{-R}$ catalysts. Based on these findings, schematics for CO adsorption and the surface structures of the catalysts were proposed (Fig. 5d). Schematics for the synthesis of the trimetallic catalysts and their surface structures are shown in Fig. S10. The use of only NaOH as the precipitant resulted in the formation of large spherical particles, whose surfaces exposed large areas of metallic Ni^0 with steps and edges. By contrast, the use of NaOH and Na_2CO_3 as coprecipitants promoted the formation of needle-like nanorods on which highly coordinated Ni^0 terrace sites were exposed.

3.2. Catalyst evaluation

FFA conversion was performed over various catalysts in ethanol at 160 $^\circ\text{C}$ and at an initial H_2 pressure of 3 MPa for 6 h (Table 2). In the absence of a catalyst, negligible FFA conversion occurred in ethanol (Fig. S11). When amorphous Al_2O_3 was used, FFA was completely converted, producing FOL in a high yield (90.3%) with a small amount of THFOL (4.2%, Fig. S12a). A similar result was obtained over commercially available $\gamma\text{-Al}_2\text{O}_3$ (Table S9). The ability of alumina to facilitate double-bond saturation has been demonstrated previously [70, 71]. Moreover, the hydrogenation activity of alumina can be attributed to dissociative H_2 adsorption on three coordinate aluminum (Al_{III}) or four-coordinate alumina centers (Al_{IV}) [72]. Because the dehydration activity of $\gamma\text{-Al}_2\text{O}_3$ was higher than that of amorphous Al_2O_3 , difurfuryl ether was produced as a byproduct (Fig. S12b). Compared with amorphous Al_2O_3 , the NiO catalyst produced FOL in a lower yield (60.4%) with byproducts such as 1-cyclohexene-1-carboxylic acid, an ethylated furan derivative, and 2-butylfuran (Fig. S13a). FFA conversion over Co_3O_4 resulted in 34.5% 1,5-PDO and 40.3% THFOL with byproducts such as 1,3-PDO, 2-PeOH, and 1-PeOH (Fig. S13b). Similar to NiO, the CoO catalyst produced a lower yield of FOL (73.4%) than amorphous Al_2O_3 , with small amounts of THFOL, 2-PeOH, 1-PeOH, and difurfuryl ether (Fig. S13c). To examine the role of the metal oxide and metallic sites in the monometallic catalysts toward the FFA conversion, in situ reduced 20 wt% $\text{Ni}/\gamma\text{-Al}_2\text{O}_3$ and 15 wt% $\text{Co}/\gamma\text{-Al}_2\text{O}_3$ catalysts were tested (Table S9). The 20 wt% $\text{Ni}/\gamma\text{-Al}_2\text{O}_3$ catalyst produced THFOL in a high yield (98.5%), whereas FFA conversion over the 15 wt% $\text{Co}/\gamma\text{-Al}_2\text{O}_3$ catalyst was less selective, yielding 59.8% THFOL, 19.1% 1, 5-PDO, 12.5% 2-PeOH, and other minor products (Fig. S14). These results suggest that alumina and metallic sites (Ni^0 , Co^0) favor C=O bond hydrogenation and subsequent furan ring saturation to produce THFOL, whereas the $\text{Co}^{\delta+}$ sites in Co_3O_4 favor the formation of ring-opened products.

As in the case of the 20 wt% $\text{Ni}/\gamma\text{-Al}_2\text{O}_3$ catalyst, the bimetallic $\text{N}_8\text{A}_1(1:2)\text{-OR}$ catalyst produced THFOL as the major product (96.0%, Table 2 and Fig. S15a). This result confirms that the presence of exposed Ni^0 sites facilitated C=O bond hydrogenation and furan ring saturation. Compared with amorphous Al_2O_3 , the $\text{C}_8\text{A}_1(1:2)\text{-OR}$ catalyst produced a higher yield of THFOL, indicating that furan ring saturation was

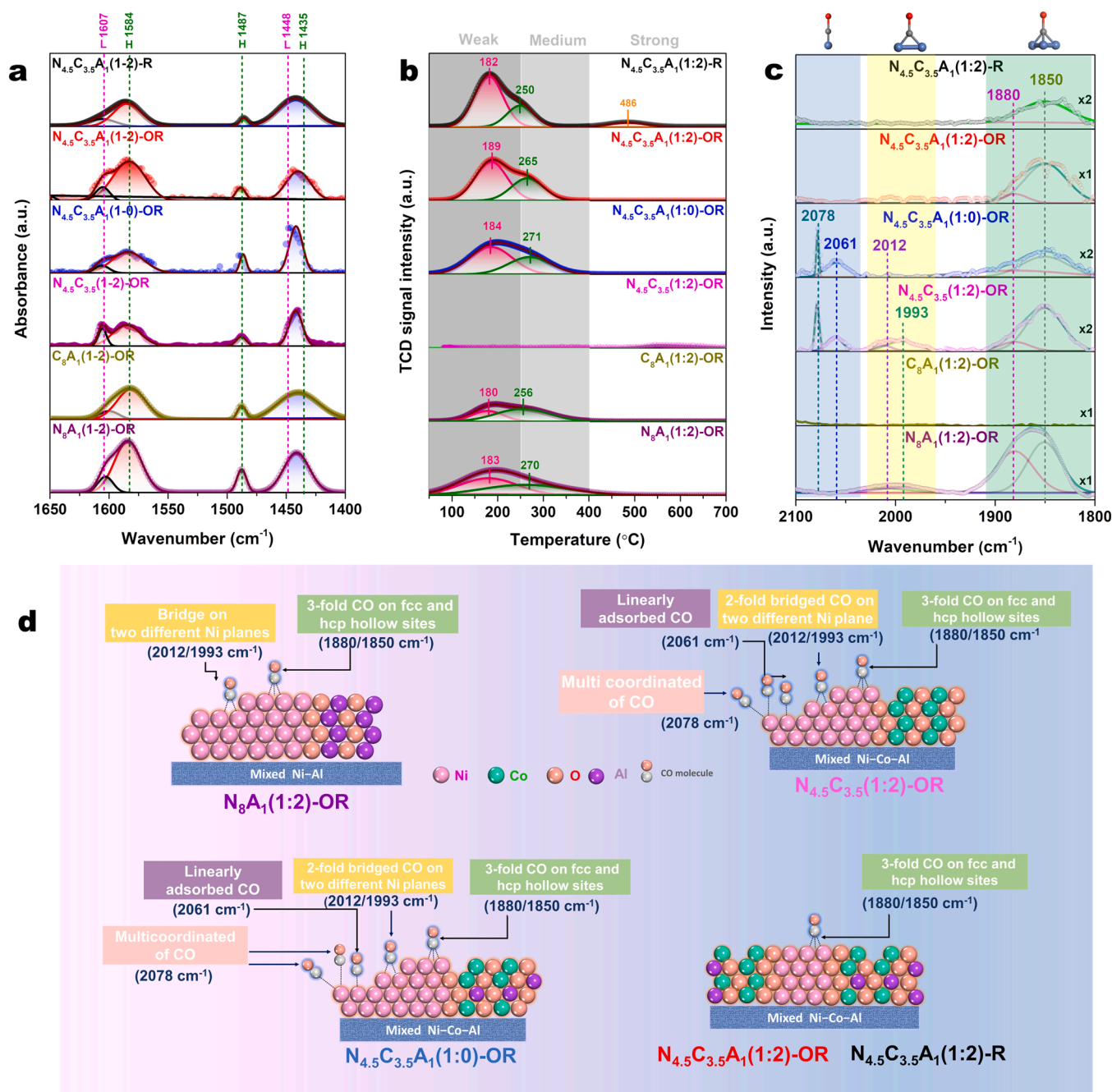


Fig. 5. (a) Pyridine-DRIFT, (b) NH₃-TPD, and (c) CO-DRIFT profiles of the bimetallic and trimetallic catalysts. (d) Schematics of the surface structures of the catalysts.

somewhat enhanced in the presence of Co^{δ+} sites. The other minor products, including difurfuryl ether and 2-furaldehyde diethyl acetal, could be produced by acid-catalyzed condensation reactions (Fig. S15b). The Ni⁰ sites in the $N_{4.5}C_{3.5}(1:2)-OR$ catalyst also facilitated FFA conversion to THFOL (Fig. S15c).

As the Al ratio in the trimetallic $N_{4.5}C_{3.5}Al_2(1:2)-OR$ catalysts increased from 0.25 to 1, the 1,5-PDO yield increased from 28.1% to 41.2%, while the THFOL yield decreased from 41.8% to 35.7%. Further increasing the Al ratio to 1.5 marginally increased the 1,5-PDO yield to 44.6%. Thus, higher Al contents in the trimetallic catalysts suppressed furan ring saturation but activated cleavage of the C₂-O bond in FOL (Fig. 1). The suppression of furan ring saturation indicates that alumina loading decreased the amount of metallic Ni⁰ domains exposed on the surface. Furthermore, over the trimetallic $N_{4.5}C_{3.5}Al_2(1:2)-OR$ catalysts,

12.4–18.9% 1,2-PDO, 3.8–5.1% 2-PeOH, and 2.3–4.1% 1-PeOH were produced. Therefore, cleavage of the C₅-O bond in FOL (Fig. 1) and subsequent C=C saturation to form 1,2-PDO, hydrogenolysis of C₁-OH in 1,2-PDO to form 2-PeOH, and hydrogenolysis of C₁-OH or C₅-OH in 1,5-PDO to form 1-PeOH occurred over the $N_{4.5}C_{3.5}Al_2(1:2)-OR$ catalysts. By contrast, when the impregnated 20 wt% Ni–15 wt% Co/ γ -Al₂O₃ catalyst was used, THFOL was the major product (92.9%) with small amounts of difurfuryl ether and 2-furaldehyde diethyl acetal (Table S9 and Fig. S16). The selective production of THFOL over the $Ni_{4.5}-Co_{3.5}/\gamma$ -Al₂O₃ catalyst is attributed to extensive furan ring saturation over Ni⁰ and Co⁰ sites. Thus, the high 1,5-PDO selectivity over the $N_{4.5}C_{3.5}Al_1(1:2)-OR$ catalyst confirms that few exposed Ni⁰ sites were present on the catalyst surface (Table S2).

To determine the optimum catalyst composition for producing 1,5-

Table 2FFA conversion and product yields over monometallic, bimetallic, and trimetallic catalysts.^a

Entry	Catalyst ^b	X _{FFA} ^c (%)	Y _{FOL} ^d (mol%)	Y _{THFOL} ^d	Y _{1,5-PDO} ^d	Y _{1,2-PDO} ^d	Y _{2-PeOH} ^d	Y _{1-PeOH} ^d	Y _{others} ^{de}
1	Blank	3.0	N.D. ^f	N.D.	N.D.	N.D.	N.D.	N.D.	3.0
2	Amorphous Al ₂ O ₃	100	90.3	4.2	N.D.	N.D.	N.D.	N.D.	5.5
3	NiO	100	60.4	Trace	N.D.	N.D.	N.D.	N.D.	39.6
4	Co ₃ O ₄	100	N.D.	40.3	34.5	10.3	3.8	1.9	9.2
5	CoO	95.6	73.4	6.7	N.D.	N.D.	1.8	0.25	12.4
6	N ₈ A ₁ (1:2)-OR	100	N.D.	96.0	N.D.	N.D.	N.D.	N.D.	4.0
7	C ₈ A ₁ (1:2)-OR	100	78.3	19.8	N.D.	N.D.	N.D.	N.D.	1.0
8	N _{4.5} C _{3.5} (1:2)-OR	100	N.D.	99.0	N.D.	N.D.	N.D.	N.D.	1.0
9	N _{4.5} C _{3.5} A _{0.25} (1:2)-OR	100	N.D.	41.8	28.1	12.4	4.2	3.3	10.2
10	N _{4.5} C _{3.5} A _{0.5} (1:2)-OR	100	N.D.	36.9	34.1	17.3	3.8	3.5	4.4
11	N _{4.5} C _{3.5} A ₁ (1:2)-OR	100	N.D.	35.7	41.2	13.0	5.1	4.1	0.8
12	N _{4.5} C _{3.5} A _{1.25} (1:2)-OR	100	N.D.	28.9	38.0	18.9	4.6	3.3	6.7
13	N _{4.5} C _{3.5} A _{1.5} (1:2)-OR	100	N.D.	28.5	44.6	17.5	4.1	2.3	3.0
15	N ₇ C ₁ A ₁ (1:2)-OR	100	N.D.	90.0	4.2	2.5	0.7	0.6	2.0
15	N ₄ C ₄ A ₁ (1:2)-OR	100	N.D.	45.0	33.2	10.0	4.3	2.6	4.9
16	N ₁ C ₇ A ₁ (1:2)-OR	100	80.0	5.1	N.D.	N.D.	N.D.	N.D.	14.9
17	N _{4.5} C _{3.5} A ₁ (1:0)-OR	100	80.2	N.D.	N.D.	N.D.	N.D.	N.D.	19.9
18	N _{4.5} C _{3.5} A ₁ (0:1)-OR	100	N.D.	33.3	39.5	18.2	4.2	2.5	2.3
19	N _{4.5} C _{3.5} A ₁ (1:2)-R	100	N.D.	24.5	47.5	19.2	4.8	3.9	0.1

^a Reaction conditions: 0.2 g of FFA, 0.1 g of catalyst, 40 mL of ethanol, 160 °C, initial H₂ pressure of 3.0 MPa, and 6 h.^b N_xC_yA_z(a:b)-OR/R; N = Ni, C = Co, A = alumina, x, y, z = weight ratio of Ni:Co:Al, OR = oxidation followed by reduction, R = reduction, a:b = molar ratio NaOH and Na₂CO₃.^c Conversion.^d Product yield.^e Y_{others} = 100 - (Y_{FOL} + Y_{THFOL} + Y_{1,5-PDO} + Y_{1,2-PDO} + Y_{2-PeOH} + Y_{1-PeOH}).^f N.D.: not detected.

PDO in a high yield, the nickel and cobalt loadings of the N_xC_yA₁(1:2)-OR catalysts were varied (Table 2). Over Ni-rich N₇C₁A₁(1:2)-OR and Co-rich N₁C₇A₁(1:2)-OR catalysts, the major products were THFOL (90.0%) and FOL (80.0%), respectively. Thus, the exposure of excess Ni⁰ domains on the catalyst surface facilitated furan ring saturation, whereas the negligibly small Ni⁰ domains in the Co-rich catalyst activated the partial hydrogenation of FFA to FOL. Over the N₄C₄A₁(1:2)-OR catalyst with equivalent Ni and Co contents, the THFOL yield decreased to 45.0%, whereas the 1,5-PDO and 1,2-PDO yields increased to 33.2% and 10.0%, respectively. The slightly Ni-rich N_{4.5}C_{3.5}A₁(1:2)-OR catalyst exhibited a higher 1,5-PDO yield of 41.2% (Fig. S17). As discussed in Section 3.1, only a very small fraction of metallic Ni⁰ was exposed on the surface of the N_{4.5}C_{3.5}A₁(1:2)-OR catalyst (2.44 area%, Table S2), which suppressed THFOL formation. In addition, the abundance of O_v sites in the CoO_x domains could activate FFA adsorption and ring-opening reactions. The role of O_v sites in 1,5-PDO formation is discussed in detail in Section 3.4.

To understand the role of precipitants in catalytic performance, the N_{4.5}C_{3.5}A₁ catalysts synthesized with NaOH or Na₂CO₃ were tested for FFA conversion. Although discrete Ni⁰ domains were formed in the N_{4.5}C_{3.5}A₁(1:0)-OR catalyst synthesized using NaOH only (Table S2), FOL was the major product (80.2%, Fig. S18). The alumina-free N_{4.5}C_{3.5}(1:2)-OR catalyst, which produced THFOL as the major product (99.0%), contained a similar amount of exposed Ni⁰ on the surface. Thus, the presence of amorphous Al₂O₃ in the N_{4.5}C_{3.5}A₁(1:0)-OR catalyst suppressed the parallel adsorption of the furan ring. Instead, tilted or perpendicular adsorption with a η¹-(O)-aldehyde configuration occurred, which facilitated the hydrogenation of just the C=O group in FFA. Over the N_{4.5}C_{3.5}A₁(0:1)-OR catalyst synthesized with Na₂CO₃ only, the yields of THFOL (33.3%) and 1,5-PDO (39.5%) were slightly lower than those over the N_{4.5}C_{3.5}A₁(1:2)-OR catalyst. These results imply that FFA molecules could be adsorbed in not only the η¹-(O)-aldehyde configuration but also the η²-(C=O)-aldehyde configuration on the surface of N_{4.5}C_{3.5}A₁(1:2)-OR, despite this catalyst having fewer exposed Ni⁰ sites than N_{4.5}C_{3.5}A₁(1:0)-OR (Table S2).

The coprecipitated catalyst precursors were calcined to remove potential organic contaminants. To examine the possibility of omitting the

calcination step during catalyst synthesis, N_{4.5}C_{3.5}A₁(1:2)-R was prepared by directly reducing the coprecipitated precursor at 400 °C under a 5% H₂/Ar flow. FFA conversion over the N_{4.5}C_{3.5}A₁(1:2)-R catalyst gave the highest 1,5-PDO yield (47.5%), while greatly suppressing THFOL formation (Table 2 and Fig. S19). Although slightly more Ni⁰ sites were exposed on the catalyst surface than in the N_{4.5}C_{3.5}A₁(1:2)-OR catalyst (Table S2), the parallel adsorption of FFA molecules was suppressed, likely because the smaller Ni⁰ domains formed by suppressing inevitable NiO particle agglomeration during calcination. In addition, the N_{4.5}C_{3.5}A₁(1:2)-R catalyst had a higher abundance of O_v-CoO_x sites (Table S6), which can facilitate 1,5-PDO formation, as discussed in detail in Section 3.4.

3.3. Optimization of reaction conditions

Reaction parameters such as calcination temperature, reaction pressure, reaction temperature, and reaction time were varied to maximize the 1,5-PDO yield over the N_{4.5}C_{3.5}A₁(1:2)-R catalyst. As the reaction temperature increased from 120 °C to 160 °C, the 1,5-PDO yield increased from 1.0% to 47.5%, whereas a further increase to 180 °C slight decreased the 1,5-PDO yield to 45.6% (Fig. 6a). Thus, high temperatures suppressed THFOL formation but activated 1,2-PDO, 1-PeOH, and 2-PeOH formation via hydrogenolysis. The N_{4.5}C_{3.5}A₁(1:2)-OR catalyst exhibited similar reaction behaviors with changing temperatures; as the temperature increase from 120 °C to 160 °C, the 1,5-PDO yield increased from 1.0% to 41.2%, while a further increase to 180 °C slight decreased the 1,5-PDO yield to 38.3% because the formation of 1,2-PDO, 2-PeOH, and 1-PeOH was activated at higher temperature (Fig. S21a). In case of the N_{4.5}C_{3.5}A₁(1:0)-OR catalyst, FOL was the major product at temperatures in the range of 120–180 °C without forming 1,5-PDO (Fig. S21c).

At a low initial H₂ pressure of 1.0 MPa, FFA was mostly converted to FOL over the N_{4.5}C_{3.5}A₁(1:2)-R catalyst, indicating that furan ring opening and ring saturation were not activated. Increasing the initial H₂ pressure to 3.0 MPa increased the 1,5-PDO yield to 47.5%, but further increments did not change the product distribution significantly (Fig. 6b). The N_{4.5}C_{3.5}A₁(1:2)-OR catalyst exhibited similar reaction

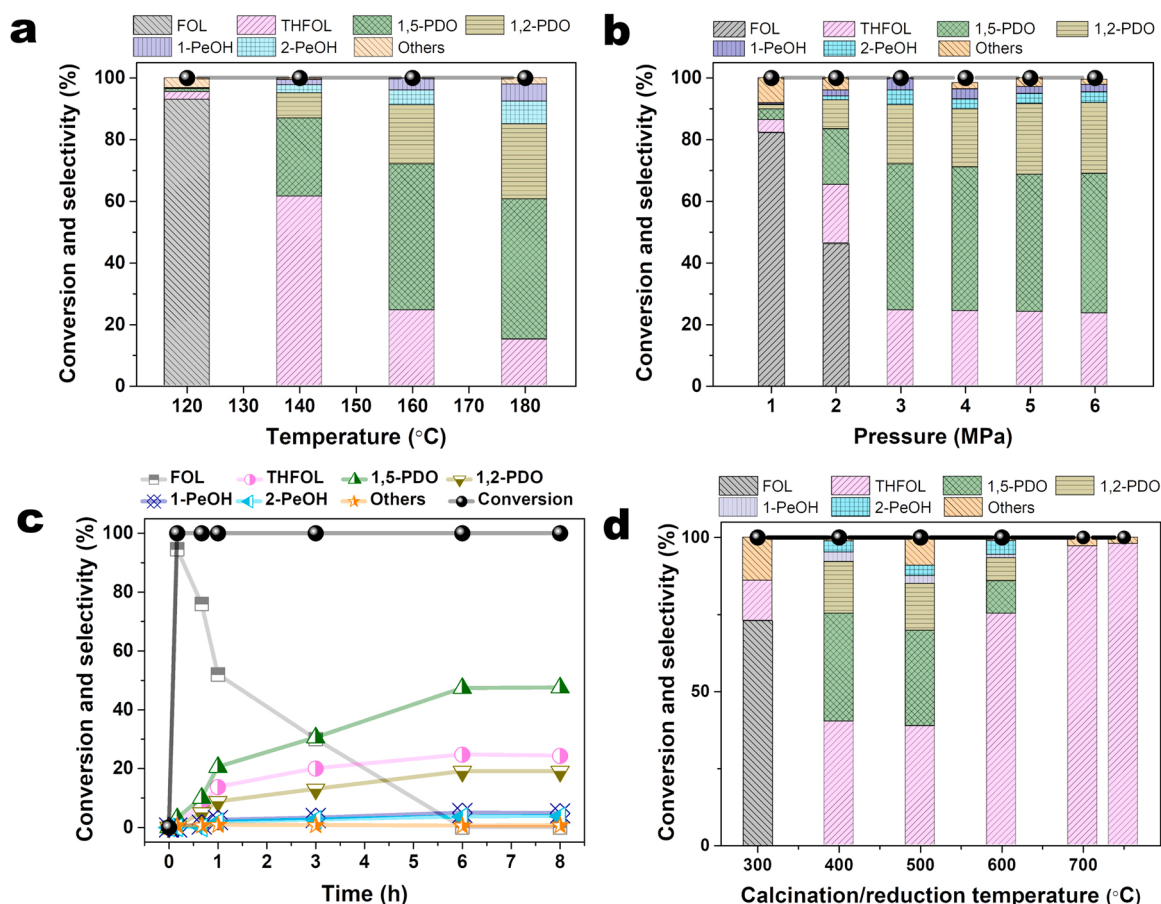


Fig. 6. FFA conversion and product yields at varying (a) reaction temperatures (reaction conditions: 0.2 g of FFA, 0.1 g of $N_{4.5}C_{3.5}A_1(1:2)\text{-R}$, 40 mL of ethanol, initial H_2 pressure of 3.0 MPa, and 6 h), (b) reaction pressures (reaction conditions: 0.2 g of FFA, 0.1 g of $N_{4.5}C_{3.5}A_1(1:2)\text{-R}$, 40 mL of ethanol, 160 °C, and 6 h), (c) reaction times (reaction conditions: 0.2 g of FFA, 0.1 g of $N_{4.5}C_{3.5}A_1(1:2)\text{-R}$, 40 mL of ethanol, initial H_2 pressure of 3.0 MPa, and 160 °C), and (d) calcination temperatures (reaction conditions: 0.2 g of FFA, 0.1 g of $N_{4.5}C_{3.5}A_1(1:2)\text{-OR}$, 40 mL of ethanol, initial H_2 pressure of 3.0 MPa, 160 °C, and 6 h).

behaviors with varying initial H_2 pressures (Fig. S21b). In case of the $N_{4.5}C_{3.5}A_1(1:0)\text{-OR}$ catalyst, the increase in the initial H_2 pressure to 6.0 MPa did not form 1,5-PDO, while FOL remained as the major product.

To clarify the reaction pathway for FFA conversion to 1,5-PDO, the evolution of the reaction intermediates and products was monitored at varying reaction times (Fig. 6c). After 10 min, FFA was completely converted, with FOL as the major product. As the reaction time increased to 1 h, the FOL yield decreased rapidly, whereas the 1,5-PDO, THFOL, and 1,2-PDO yields increased. Complete FOL conversion was achieved after 6 h to produce 1,5-PDO (47.5%), 1,2-PDO (19.2%), 1-PeOH (4.8%), and 2-PeOH (3.9%). However, the product distribution did not change significantly upon increasing the reaction time to 8 h. Thus, the C=O bond in FFA was initially hydrogenated to produce FOL, which subsequently reacted via competing $C_2\text{-O}$ and $C_5\text{-O}$ bond cleavage and furan ring saturation pathways. The possibility of THFOL conversion to 1,5-PDO was excluded because THFOL did not react over the $N_{4.5}C_{3.5}A_1(1:2)\text{-R}$ catalyst (Fig. S20 and Table S10).

The calcination and reduction temperatures of the coprecipitated catalyst precursors had a significant effect on the product yields (Fig. 6d). The $N_{4.5}C_{3.5}A_1(1:2)\text{-OR}$ catalyst calcined and reduced at 300 °C resulted in a high yield of FOL. As these low temperatures decreased the possibility of forming discrete Ni domains, thus limiting dissociative H_2 adsorption and hydrogen spillover to the CoO_x sites. Consequently, as in the case of the Ni-free $C_8A_1(1:2)\text{-OR}$ catalyst, the further conversion of FOL to ring-opened and ring-saturated products was suppressed. Increasing the calcination and reduction temperatures to 400 °C produced 1,5-PDO in a high yield (35.1%). However, when the

calcination and reduction temperatures were 750 °C, the major product was THFOL. This high-temperature treatment could form discrete metallic Ni^0 and Co^0 domains, thus facilitating the parallel adsorption of FOL, which favors the formation of the ring-saturated product. Therefore, in metal-metal oxide bifunctional catalysts, the metallic sites should be few to sufficiently suppress the parallel adsorption of FFA molecules.

3.4. DFT calculations and reaction pathways

To gain insights into the reaction mechanism, DFT calculations were performed. Fig. S22 shows the catalyst model slabs of Ni (111), pristine Co_3O_4 (110), and $O_v\text{-}Co_3O_4$ (110). When a H_2 molecule approaches the Ni (111) surface, dissociative H_2 adsorption on a Ni atom is the most favorable molecular adsorption process (Figs. S23a-c). On the pristine Co_3O_4 (110) surface, the H_2 molecule is preferentially adsorbed on a $Co^{\delta+}$ atom, whereas on the $O_v\text{-}Co_3O_4$ (110) surface, the H_2 molecule is preferentially adsorbed on a $Co^{\delta+}$ atom adjacent to an O_v site (Figs. S23d-g). After dissociation, the H atoms are strongly adsorbed on the surface fcc, hcp, and mixed fcc and hcp sites of Ni (111) with adsorption energies of -3.35 , -3.57 , and -3.46 eV, respectively (Figs. S24a-c). The H atoms are connected to three neighboring Ni atoms located 0.932 and 0.921 Å from the surface fcc and hcp sites of Ni (111) respectively. In the case of pristine Co_3O_4 (110), the H atoms are preferentially adsorbed on an O atom (adsorption energy = -3.23 eV) rather than a $Co^{\delta+}$ atom (adsorption energy = -1.87 eV). By contrast, on the $O_v\text{-}Co_3O_4$ (110) surface, H atom adsorption on two $Co^{\delta+}$ atoms that are adjacent to an O_v site (adsorption energy = -3.40 eV) is more favorable

than adsorption on an O atom (adsorption energy = -3.31 eV) (Figs. S24c-f). The reaction diagrams and energy values for dissociative H_2 adsorption on the Ni (111), Co_3O_4 (110), and $O_v-Co_3O_4$ (110) surfaces are shown in Fig. S25. On the fcc, hcp and mixed fcc-hcp sites of Ni (111) sites, the activation barriers for H_2 dissociation are low (0.141, 0.145, and 0.152 eV respectively), and spillover to the fcc, hcp, and mixed fcc-hcp adsorption sites is thermodynamically favorable because of their high negative reaction energies (-0.745 , -0.656 , and -0.717 eV, respectively). Owing to high activation barriers (0.41–0.80 eV), dissociative H_2 adsorption on the pristine Co_3O_4 (110) and $O_v-Co_3O_4$ (110) surfaces is less favorable than that on Ni (111). However, Co^{6+} atoms adjacent to O_v sites are promising for the uptake of spillover hydrogen because they can stabilize dissociated H atoms through electron donation. As revealed by the partial density of state (PDOS) profiles (Fig. S26), among the H-atom-adsorbed surfaces, the d-band center of the H atom adsorbed on Co^{6+} in the $O_v-Co_3O_4$ (110) surface is the closest to the Fermi level. Because of this reduced ability to fill the antibonding orbital of the catalyst with electrons, the strong adsorption of H atoms on the $O_v-Co_3O_4$ (110) surface is anticipated [73]. Owing to the low energy barrier for H_2 dissociation on Ni^0 and strong H atom adsorption, the $O_v-Co_3O_4$ (110) surface is promising as a hydrogenation catalyst.

The adsorption geometries of FFA and FOL on the pristine Co_3O_4 (110) and $O_v-Co_3O_4$ (110) surfaces were investigated using DFT calculations (Fig. S27). On the pristine Co_3O_4 (110) surface, FFA is preferentially adsorbed on the Co^{6+} atom in a $\eta^1-(O)-aldehyde$ configuration with a slightly tilted geometry and a distance of 2.08 Å between the Co^{6+} atom and the carbonyl oxygen (O_1) of FFA. Because the interaction between the furan ring of FFA and the Co_3O_4 (110) surface is unfavorable, the carbon atoms in the furan ring do not lose their sp^2 character. The high adsorption energy of -1.89 eV indicates a strong interaction between the O_1 atom of FFA and the Co^{6+} atom. On the $O_v-Co_3O_4$ (110) surface, FFA adsorption involves a similar tilted geometry with a distance of 2.05 Å. A high adsorption energy of -1.90 eV indicates that Co^{6+} atoms next to O_v sites are favorable adsorption sites. Similar to FFA, FOL is adsorbed on the pristine Co_3O_4 (110) and $O_v-Co_3O_4$ (110) surfaces in a $\eta^1-(O)-alcoholic$ configuration with flat and tilted geometries, respectively. The distances between the O_1 atom of FOL and the Co^{6+} atoms in the pristine Co_3O_4 (110) and $O_v-Co_3O_4$ (110) surfaces are 2.17 and 2.05 Å, respectively. The adsorption energies of FOL on the pristine Co_3O_4 (110) and $O_v-Co_3O_4$ (110) surfaces (-1.58 and -1.64 eV, respectively) were slightly lower than those of FFA. As shown in Fig. S28, the d-band centers of the FFA- and FOL-adsorbed $O_v-Co_3O_4$ (110) surfaces are closer to the Fermi level than those of the corresponding pristine Co_3O_4 (110) surfaces. Thus, the antibonding orbital formed by the metal d-band and adsorbate orbital can be more difficult to be filled with electrons, resulting in stronger adsorption on the $O_v-Co_3O_4$ (110) surface [74,75].

To understand role of oxygen vacancies in the conversion of FOL to 1,5-PDO, 1,2-PDO, and THFOL, the cleavage of the C_2-O and C_5-O bonds in FOL on the pristine Co_3O_4 (110) and $O_v-Co_3O_4$ (110) surfaces was investigated (Fig. S29). During the attack of an adsorbed H atom on the C_2 atom of FOL adsorbed on the pristine Co_3O_4 (110) surface, the C_2-O bond length increases from 1.38 to 2.11 Å. Subsequent C_2-O bond cleavage forms $HOCH_2(CH)_4O$ as an intermediate in the formation of 1,5-PDO. Attack on the C_5 atom of FOL by an adsorbed H atom and subsequent C_5-O bond cleavage produces $HOCH_2CO(CH)_2CH_2$ as an intermediate in the formation of 1,2-PDO. In the transition state, the C_5-O bond length increases from 1.37 to 2.17 Å. When the adsorbed H atom attacks the C_3 atom in the furan ring, the double bond becomes saturated, with the $C_3=C_2$ bond length increasing from 1.37 to 1.56 Å in the transition state. As shown in Fig. 7a, the activation energy barriers are in the following order: 1,2-PDO pathway (0.85 eV) > THFOL pathway (0.80 eV) > 1,5-PDO pathway (0.72 eV). In addition, the reaction energies are in the following order: 1,2-PDO pathway (-0.17 eV) > THFOL pathway (-0.72 eV) > 1,5-PDO pathway (-1.39 eV).

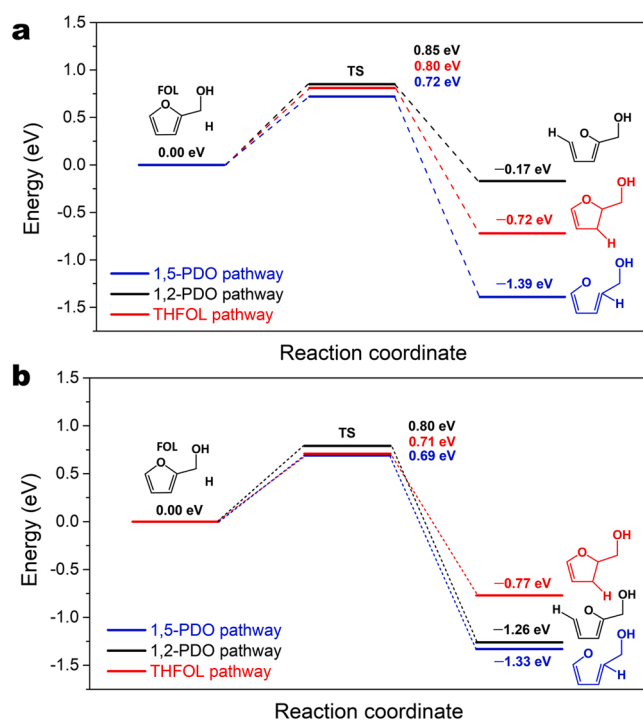


Fig. 7. Reaction coordinates for the conversion of FOL to $HOCH_2(CH)_4O$, $HOCH_2CO(CH)_2CH_2$, and $HOCH_2CCH_2(CH)_2O$ as intermediates for the synthesis of 1,5-PDO, 1,2-PDO, and THFOL, respectively, over (a) pristine Co_3O_4 (110) and (b) $O_v-Co_3O_4$ (110).

Therefore, the 1,5-PDO pathway is kinetically and thermodynamically more favorable than the 1,2-PDO and THFOL pathways on the pristine Co_3O_4 (110) surface. Electron density depletion at the C_2 atom of FOL increases its susceptibility to H attack by lowering the energy barrier for ring opening (Fig. S30a).

When the H atom attacked the C_2 , C_5 , and C_3 atoms of the $O_v-Co_3O_4$ (110) surface (Fig. S31), the C_2-O , C_5-O , and $C_3=C_2$ bonds lengthen to 2.44 , 2.20 , and 1.61 Å, respectively. As shown in Fig. 7b, the activation energy barriers are in the order of 1,2-PDO pathway (0.80 eV) > THFOL pathway (0.71 eV) > 1,5-PDO pathway (0.69 eV) and the reaction energies are in the order of THFOL pathway (-0.77 eV) > 1,2-PDO pathway (-1.26 eV) > 1,5-PDO pathway (-1.33 eV). Therefore, as in the case of the pristine Co_3O_4 (110) surface, FOL conversion to 1,5-PDO is more favorable than conversion to 1,2-PDO or THFOL on the $O_v-Co_3O_4$ (110) surface. The electron-enriched Co^{6+} atoms adjacent to the O_v sites cause the O_1 atom of FOL to be more strongly adsorbed on the $O_v-Co_3O_4$ (110) surface and the electron density of the C_2 atom of FOL adsorbed on the $O_v-Co_3O_4$ (110) surface is even more depleted than that on the pristine Co_3O_4 (110) surface (Fig. S30b). Consequently, the activation energy barrier for C_2-O cleavage over the $O_v-Co_3O_4$ (110) surface is lower than that over the pristine Co_3O_4 (110) surface.

Based on these findings, a plausible reaction pathway for the one-pot conversion of FFA to 1,5-PDO over the $N_{4.5}C_{3.5}A_1(1:2)-R$ catalyst was proposed (Fig. 8). First, H_2 molecules are dissociatively adsorbed on Ni^0 sites with subsequent spillover of H atoms to the CoO_x sites. Next, the O_1 atom in the carbonyl group of FFA is adsorbed on the Co^{6+} site in the $\eta^1-(O)-aldehyde$ configuration. Then, two H atoms attack the $C=O$ group of adsorbed FFA to produce FOL. H attack on FOL can induce C_2-O bond cleavage, C_5-O bond cleavage, or furan ring saturation. Among these competing reactions, the preferential pathway on the O_v-CoO_x surface is C_2-O bond cleavage. After ring opening, 1,5-PDO is produced by H attack on the double bond in the furan ring and the O_2 atom.

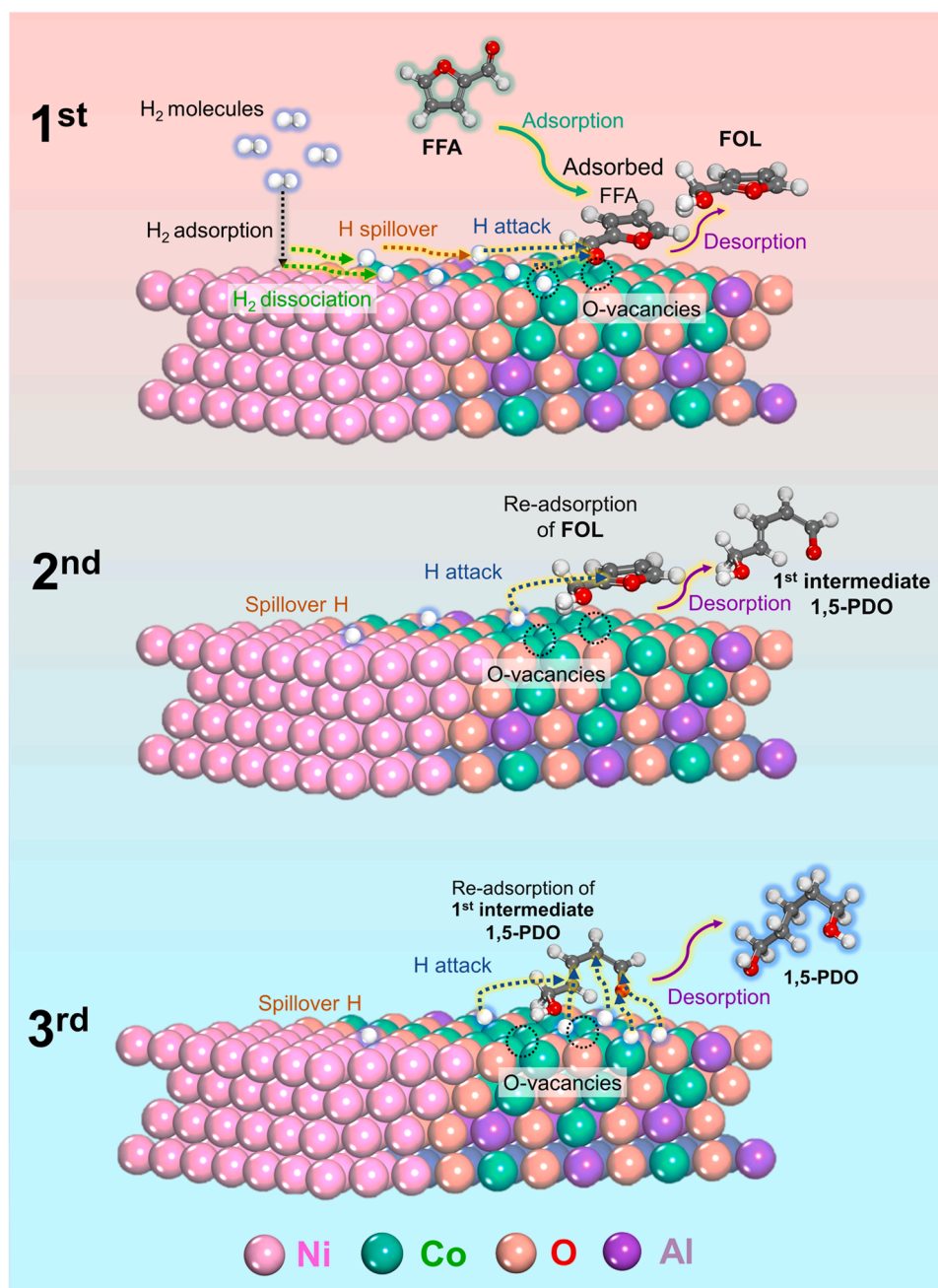


Fig. 8. Proposed reaction mechanism for the direct conversion of FFA to 1,5-PDO over the $N_{4.5}C_{3.5}A_1(1:2)$ -R catalyst.

3.5. Catalyst recyclability

To investigate the stability and reusability of the $N_{4.5}C_{3.5}A_1(1:2)$ -R catalyst, four consecutive FFA conversion cycles were performed at 160 °C with an initial H_2 pressure of 3.0 MPa for 6 h in ethanol (Fig. 9a). After each reaction, the spent catalyst was separated from the reaction mixture via centrifugation, washed with DDI water, and dried in a vacuum oven at 80 °C overnight. The dried spent catalyst was reused under identical reaction condition without additional calcination or reactivation steps. From the first to the fourth cycle, the 1,5-PDO yield gradually decreased from 47.5% to 27.0%, while the THFOL yield gradually increased from 24.5% to 54.0%.

Various factors could be responsible for this decrease in catalytic activity for 1,5-PDO production, including changes in phase or electronic structures, coke deposition on active sites, oxidation of metal active sites, loss of O_v sites, sintering of active sites, and metal leaching.

To investigate possible phase structure changes, the spent catalyst (denoted $N_{4.5}C_{3.5}A_1(1:2)$ -R-S) collected after the fourth cycle was analyzed using XRD (Fig. 9b). The intensities of the peaks at 43.2° and 62.9°, which correspond to the (200) and (220) planes of NiO, respectively, are maintained. However, the CoO (111) peak at 36.2° disappears, indicating that CoO was oxidized to Co_3O_4 during the reaction. The surface electronic structures of the spent catalyst were analyzed using XPS (Fig. 9c). The Ni^0 peak detected at 852.7 eV for the fresh catalyst is not observed for the $N_{4.5}C_{3.5}A_1(1:2)$ -R-S catalyst. In addition, the ratio of Co^{3+} (Co_3O_4) and Co^{2+} (CoO) increases from 0.97 (fresh) to 1.09 (spent). Thus, some degree of surface oxidation occurred during the reaction. The Co K-edge XANES and k^3 -weighted Fourier-transform magnitudes of the Co K-edge EXAFS spectra of the fresh and spent catalysts are similar (Fig. 9d and e). However, the CNs of Co-O and Co-O-Co in the CoO phase decrease from 4.4 (fresh) to 4.2 (spent) and 6.9 (fresh) to 5.0 (spent), respectively. In addition, the CN of Co-O in of

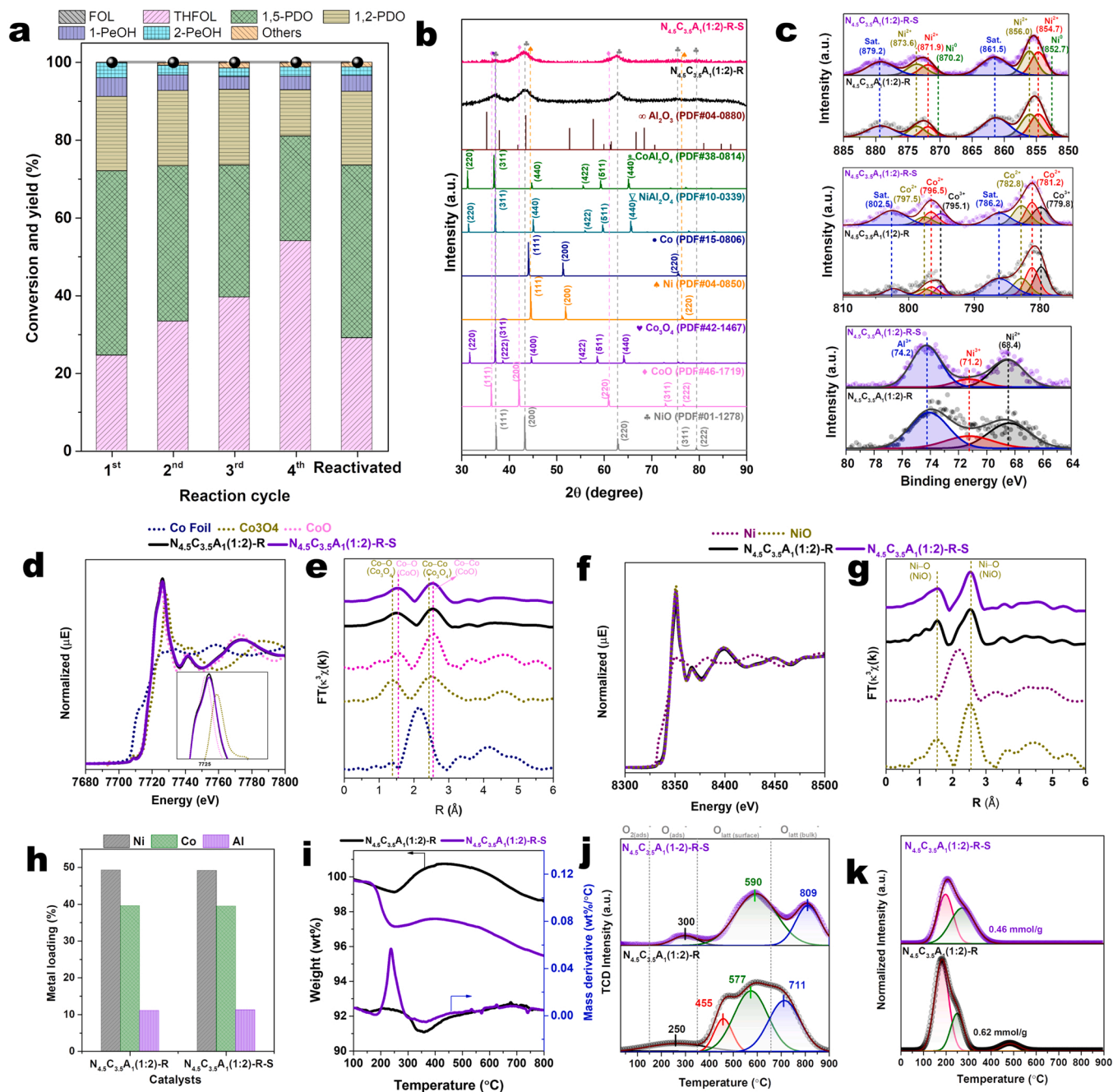


Fig. 9. (a) Reusability of the $N_{4.5}C_{3.5}A_1(1:2)-R$ catalyst for FFA conversion. Reaction conditions: 0.2 g of FFA, 0.1 g of catalyst, 40 mL of ethanol, 160 °C, initial H_2 pressure of 3.0 MPa, and 6 h. (b) XRD patterns, (c) XPS profiles, normalized (d) Co K-edge and (f) Ni K-edge XANES spectra, and k^3 -weighted Fourier transforms of the normalized (e) Co K-edge and (g) Ni K-edge EXAFS spectra ($\kappa^3\chi(k)$), (h) ICP-OES data, (i) TGA profiles, (j) NH_3 -TPD profiles, and (k) O_2 -TPD of fresh $N_{4.5}C_{3.5}A_1(1:2)-R$ and spent $N_{4.5}C_{3.5}A_1(1:2)-R$ catalysts.

the Co_3O_4 phase slightly increases from 0.8 (fresh) to 1.2 (spent). The local chemical environment of the bulk NiO phase does not change significantly (Fig. 9 f and g). However, based on the linear combination fitting results and the Ni loading data obtained using ICP-OES (Fig. 9 h), the Ni^0 content in the spent catalyst is lower (0.46 wt%) than that in the fresh catalyst (1.7 wt%). Nevertheless, negligible metal leaching occurs during the reaction, indicating the high structural stability of the catalyst. The TGA profiles of the fresh and spent catalysts are shown in Fig. 9i. The fresh catalyst exhibits a weight loss of approximately 1 wt% upon increasing the temperature to 250 °C. In the temperature range of 250–460 °C, the weight gain of 1.6 wt% for the fresh catalyst is attributed to the oxidation of Ni^0 and oxygen uptake at the O_v sites. Further

increasing the temperature to 800 °C resulted in a weight loss due to the deformation of the oxygen bulk lattice of Co_3O_4 [56]. The spent catalyst exhibits a small weight loss (1.8 wt%) in the temperature range of 200–300 °C, which is attributed to the combustion of the organics remaining on the catalyst surface. The weight gain at 300–500 °C, caused by the oxidation of Ni^0 and O_v sites during the reaction, is smaller for the spent catalyst (0.4 wt%) than for the fresh catalyst (1.6 wt%). As shown in Fig. 9j, less oxygen is desorbed from the lattice oxygen sites at the surface in the spent catalyst (0.268 mmol g_{Co}^{-1}) than from the fresh catalyst (0.399 mmol g_{Co}^{-1}). Organic coverage and the loss of O_v sites on the spent catalyst caused the acidity of the spent catalyst (0.46 mmol g^{-1}) to be lower than that of the fresh catalyst

(0.62 mmol g⁻¹) (Fig. 9k).

These findings indicate that the loss of catalytic activity was mainly due to the oxidation of metallic Ni⁰ and O_v sites. To examine the possibility of catalyst reactivation, the spent N_{4.5}C_{3.5}A₁(1:2)-R-S catalyst collected after the fourth run was dried and then reduced under a flow of 5% H₂/Ar at 400 °C for 4 h. When the reactivated catalyst was applied to FFA conversion, the initial activity of the fresh N_{4.5}C_{3.5}A₁(1:2)-R catalyst was regained (Fig. 9a), indicating the high stability and reusability of this catalyst.

4. Conclusion

In summary, the trimetallic Ni-CoO_x-Al₂O₃ mixed metal-metal oxide catalyst was highly efficient for the one-pot direct conversion of FFA to 1,5-PDO in a high yield (47.5%) at 160 °C with an initial H₂ pressure of 3 MPa for 6 h in ethanol. The presence of amorphous alumina hindered the growth of metallic Ni⁰ phases, thus suppressing the parallel adsorption of FFA and subsequent furan ring saturation. The amount of surface-exposed ultrasmall Ni⁰ domain was sufficient to facilitate the dissociative adsorption of H₂ molecules. The dissociated H atoms were subsequently transferred to oxygen-vacant CoO_x (O_v-CoO_x) sites by a hydrogen spillover mechanism. On electron-enriched Co^{δ+} centers adjacent to O_v sites, FFA was strongly adsorbed in the η¹-(O)-aldehyde configuration, which allowed the H atom to attack the C=O group to produce FOL. Then, the C₂-O bond in FOL adsorbed on the Co^{δ+} center of CoO_x was cleaved to produce 1,5-PDO, as this pathway was both kinetically and thermodynamically more favorable than C₅-O bond cleavage to form 1,2-PDO and furan ring saturation to form THFOL. DFT calculations revealed that more electron-enriched Co^{δ+} centers adjacent to the O_v sites increased the adsorption strength of the hydroxyl O atom of FOL and the electron density of the C₂ atom of FOL adsorbed on the Co^{δ+} center was more depleted than that adsorbed on the pristine Co₃O₄ (110) surface, resulting in the C₂-O bond cleavage. Recyclability tests revealed that the oxidation of Ni⁰ sites and oxygen uptake at the O_v sites were the main deactivation mechanisms; thus, reactivation under H₂ conditions restored the initial activity of the trimetallic Ni-CoO_x-Al₂O₃ catalyst. Overall, the trimetallic Ni-CoO_x-Al₂O₃ catalyst was prepared from inexpensive starting materials, produced 1,5-PDO in a high yield, and exhibited high stability. Thus, this catalytic system is highly promising and economically viable for the production of 1,5-PDO directly from FFA.

CRediT authorship contribution statement

Rizky Gilang Kurniawan: Conceptualization, Methodology, Formal analysis, Data curation, Writing – original draft. **Neha Karanwal:** Methodology, Investigation, Data curation. **Jaeyong Park:** Validation, Formal analysis, Investigation. **Deepak Verma:** Methodology, Formal analysis, Investigation. **Sang Kyu Kwak:** Conceptualization, Methodology, Investigation. **Seok Ki Kim:** Conceptualization, Methodology, Investigation. **Jaehoon Kim:** Supervision, Project administration, Resources, Writing – review & editing, Funding acquisition.

Declaration of Competing Interest

The authors declare that they have no known competing financial interests or personal relationships that could have appeared to influence the work reported in this paper.

Data Availability

Data will be made available on request.

Acknowledgements

This research was supported by the Bio & Medical Technology

Development Program of the National Research Foundation (NRF) funded by the Korean government through the Ministry of Science and ICT (MSIT) (No. 2022M3A9F3017700). Additional support was provided by NRF grants funded by MSIT (Nos. 2020M1A2A2080430 and 2020H1D3A2A02085762). We used the 8 C synchrotron beamline of the Pohang Accelerator Laboratory (Republic of Korea) under contact no. 2021–3rd-8 C-010.

Appendix A. Supporting information

Supplementary data associated with this article can be found in the online version at doi:10.1016/j.apcatb.2022.121971.

References

- [1] J. Pang, J. Sun, M. Zheng, H. Li, Y. Wang, T. Zhang, Transition metal carbide catalysts for biomass conversion: a review, *Appl. Catal. B* 254 (2019) 510–522, <https://doi.org/10.1016/j.apcatb.2019.05.034>.
- [2] S. Kim, Y.F. Tsang, E.E. Kwon, K.-Y.A. Lin, J. Lee, Recently developed methods to enhance stability of heterogeneous catalysts for conversion of biomass-derived feedstocks, *Korean J. Chem. Eng.* 36 (2019) 1–11, <https://doi.org/10.1007/s11814-018-0174-x>.
- [3] R. Mariscal, P. Maireles-Torres, M. Ojeda, I. Sádaba, M.L. Granados, Furfural: a renewable and versatile platform molecule for the synthesis of chemicals and fuels, *Energy Environ. Sci.* 9 (2016) 1144–1189, <https://doi.org/10.1039/C5EE02666K>.
- [4] R. Insyani, A.F. Barus, R. Gunawan, J. Park, G.T. Jaya, H.S. Cahyadi, M.G. Sibi, S. K. Kwak, D. Verma, J. Kim, RuO₂-Ru/H β zeolite catalyst for high-yield direct conversion of xylose to tetrahydrofurfuryl alcohol, *Appl. Catal. B* 291 (2021), 120120, <https://doi.org/10.1016/j.apcatb.2021.120120>.
- [5] W. Xu, H. Wang, X. Liu, J. Ren, Y. Wang, G. Lu, Direct catalytic conversion of furfural to 1, 5-pentanediol by hydrogenolysis of the furan ring under mild conditions over Pt/Co₂AlO₄ catalyst, *ChemComm* 47 (2011) 3924–3926, <https://doi.org/10.1039/C0CC05775D>.
- [6] K. Huang, Z.J. Brentzel, K.J. Barnett, J.A. Dumesic, G.W. Huber, C.T. Maravelias, Conversion of furfural to 1, 5-pentanediol: Process synthesis and analysis, *ACS Sustain. Chem. Eng.* 5 (2017) 4699–4706, <https://doi.org/10.1021/acscuschemeng.7b00059>.
- [7] Daily Media, Energy Siren, 2022, <https://energysiren.co.ke/2022/03/06/15-pentanediol-market-valued-at-28-05-mn-in-2021-will-grow-with-a-cagr-of-3-73-from-2022-to-2028-2/> (accessed 22 August 2022).
- [8] S. Koso, N. Ueda, Y. Shinmi, K. Okumura, T. Kizuka, K. Tomishige, Promoting effect of Mo on the hydrogenolysis of tetrahydrofurfuryl alcohol to 1,5-pentanediol over Rh/SiO₂, *J. Catal.* 267 (2009) 89–92, <https://doi.org/10.1016/j.jcat.2009.07.010>.
- [9] S. Koso, I. Furikado, A. Shimao, T. Miyazawa, K. Kunimori, K. Tomishige, Chemoselective hydrogenolysis of tetrahydrofurfuryl alcohol to 1, 5-pentanediol, *Chem. Comm.* (2009) 2035–2037, <https://doi.org/10.1039/B822942B>.
- [10] S. Koso, Y. Nakagawa, K. Tomishige, Mechanism of the hydrogenolysis of ethers over silica-supported rhodium catalyst modified with rhenium oxide, *J. Catal.* 280 (2011) 221–229, <https://doi.org/10.1016/j.jcat.2011.03.018>.
- [11] M. Chia, Y.J. Pagán-Torres, D. Hibbitts, Q. Tan, H.N. Pham, A.K. Datye, M. Neurock, R.J. Davis, J.A. Dumesic, Selective hydrogenolysis of polyols and cyclic ethers over bifunctional surface sites on rhodium–rhenium catalysts, *J. Am. Chem. Soc.* 133 (2011) 12675–12689, <https://doi.org/10.1021/ja2038358>.
- [12] K. Chen, K. Mori, H. Watanabe, Y. Nakagawa, K. Tomishige, C–O bond hydrogenolysis of cyclic ethers with OH groups over rhenium-modified supported iridium catalysts, *J. Catal.* 294 (2012) 171–183, <https://doi.org/10.1016/j.jcat.2012.07.015>.
- [13] Z. Wang, B. Pholjaroen, M. Li, W. Dong, N. Li, A. Wang, X. Wang, Y. Cong, T. Zhang, Chemoselective hydrogenolysis of tetrahydrofurfuryl alcohol to 1,5-pentanediol over Ir-MoO_x/SiO₂ catalyst, *J. Energy Chem.* 23 (2014) 427–434, [https://doi.org/10.1016/S2095-4956\(14\)60168-6](https://doi.org/10.1016/S2095-4956(14)60168-6).
- [14] S. Feng, A. Nagao, T. Aihara, H. Miura, T. Shishido, Selective hydrogenolysis of tetrahydrofurfuryl alcohol on Pt/WO₃/ZrO₂ catalysts: Effect of WO₃ loading amount on activity, *Catal. Today* 303 (2018) 207–212, <https://doi.org/10.1016/j.cattod.2017.08.058>.
- [15] B. Kuang, Q. Zhang, Y. Fang, Y. Bai, S. Qiu, P. Wu, Y. Qin, T. Wang, Ring opening of cyclic ether for selective synthesis of renewable 1, 5-pentanediol over Pt/WO₃@SiO₂ catalysts, *Ind. Eng. Chem. Res.* 59 (2020) 9372–9381, <https://doi.org/10.1021/acs.iecr.9b06790>.
- [16] K. Chen, S. Koso, T. Kubota, Y. Nakagawa, K. Tomishige, Chemoselective hydrogenolysis of tetrahydrofuran-2-methanol to 1, 6-hexanediol over rhenium-modified carbon-supported rhodium catalysts, *ChemCatChem* 2 (2010) 547–555, <https://doi.org/10.1002/cctc.201000018>.
- [17] B. Pholjaroen, N. Li, Y. Huang, L. Li, A. Wang, T. Zhang, Selective hydrogenolysis of tetrahydrofurfuryl alcohol to 1,5-pentanediol over vanadium modified Ir/SiO₂ catalyst, *Catal. Today* 245 (2015) 93–99, <https://doi.org/10.1016/j.cattod.2014.08.011>.
- [18] M. Chatterjee, H. Kawanami, T. Ishizaka, M. Sato, T. Suzuki, A. Suzuki, An attempt to achieve the direct hydrogenolysis of tetrahydrofurfuryl alcohol in supercritical carbon dioxide, *Catal. Sci. Technol.* 1 (2011) 1466–1471, <https://doi.org/10.1039/C1CY00125F>.

- [19] C. Wang, J.D. Lee, Y. Ji, T.M. Onn, J. Luo, C.B. Murray, R.J. Gorte, A Study of tetrahydrofurfuryl alcohol to 1,5-pentanediol over Pt-WO₃/C, *Catal. Lett.* 148 (2018) 1047–1054, <https://doi.org/10.1007/s10562-018-2323-6>.
- [20] Z.J. Brentzel, K.J. Barnett, K. Huang, C.T. Maravelias, J.A. Dumesic, G.W. Huber, Chemicals from biomass: combining ring-opening tautomerization and hydrogenation reactions to produce 1,5-pentanediol from furfural, *ChemSusChem* 10 (2017) 1351–1355, <https://doi.org/10.1002/cssc.201700178>.
- [21] J. He, K. Huang, K.J. Barnett, S.H. Krishna, D.M. Alonso, Z.J. Brentzel, S.P. Burt, T. Walker, W.F. Banholzer, C.T. Maravelias, New catalytic strategies for α , ω -diols production from lignocellulosic biomass, *Faraday Discuss.* 202 (2017) 247–267, <https://doi.org/10.1039/C7FD00036G>.
- [22] L. Gavilá, A. Lähde, J. Jokiniemi, M. Constanti, F. Medina, E. Río, D. Tichit, M. G. Álvarez, Insights on the one-pot formation of 1,5-pentanediol from furfural with Co–Al spinel-based nanoparticles as an alternative to noble metal catalysts, *ChemCatChem* 11 (2019) 4944–4953, <https://doi.org/10.1002/cctc.201901078>.
- [23] T.P. Sulmonetti, B. Hu, S. Lee, P.K. Agrawal, C.W. Jones, Reduced Cu–Co–Al mixed metal oxides for the ring-opening of furfuryl alcohol to produce renewable diols, *ACS Sustain. Chem. Eng.* 5 (2017) 8959–8969, <https://doi.org/10.1021/acssuschemeng.7b01769>.
- [24] S. Liu, Y. Amada, M. Tamura, Y. Nakagawa, K. Tomishige, Performance and characterization of rhenium-modified Rh–Ir alloy catalyst for one-pot conversion of furfural into 1, 5-pentanediol, *Catal. Sci. Technol.* 4 (2014) 2535–2549, <https://doi.org/10.1039/C4CY00161C>.
- [25] S. Liu, Y. Amada, M. Tamura, Y. Nakagawa, K. Tomishige, One-pot selective conversion of furfural into 1, 5-pentanediol over a Pd-added Ir–ReO_x/SiO₂ bifunctional catalyst, *Green. Chem.* 16 (2014) 617–626, <https://doi.org/10.1039/C3GC41335G>.
- [26] Rhodium prices: check live & historical rhodium spot price, Money metals, Money Metals. <https://www.moneymetals.com/rhodium-price>, 2022 (Accessed 22 August 2022).
- [27] Average monthly iridium price worldwide from March 2020 to March 2021. <https://www.statista.com/statistics/1229812/iridium-price-monthly/#:~:text=The%20average%20annual%20price%20for,U.S.%20dollars%20per%20troy%20ounce,2022> (Accessed 22 August 2022).
- [28] Current strategic metal prices, Strategic metal invest. <https://strategicmetalsinvest.com/current-strategic-metals-prices/>, 2022 (Accessed 22 August 2022).
- [29] X. Fu, X. Ren, J. Shen, Y. Jiang, Y. Wang, Y. Orooji, W. Xu, J. Liang, Synergistic catalytic hydrogenation of furfural to 1, 2-pentanediol and 1, 5-pentanediol with LDO derived from CuMgAl hydrotalcite, *Mol. Catal.* 499 (2021), 111298, <https://doi.org/10.1016/j.mcat.2020.111298>.
- [30] J. Guan, G. Peng, Q. Cao, X. Mu, Role of MoO₃ on a rhodium catalyst in the selective hydrogenolysis of biomass-derived tetrahydrofurfuryl alcohol into 1,5-pentanediol, *J. Phys. Chem. C* 118 (2014) 25555–25566, <https://doi.org/10.1021/jp508313y>.
- [31] S. Liu, Y. Amada, M. Tamura, Y. Nakagawa, K. Tomishige, Performance and characterization of rhenium-modified Rh–Ir alloy catalyst for one-pot conversion of furfural into 1,5-pentanediol, *Catal. Sci. Technol.* 4 (2014) 2535–2549, <https://doi.org/10.1039/C4CY00161C>.
- [32] T.L.M. Exchange, Precious metal. <https://www.lme.com/en/Metals>, 2021 (accessed 22 August 2022).
- [33] H. Prajitno, R. Insyani, J. Park, C. Ryu, J. Kim, Non-catalytic upgrading of fast pyrolysis bio-oil in supercritical ethanol and combustion behavior of the upgraded oil, *Appl. Energy* 172 (2016) 12–22, <https://doi.org/10.1016/j.apenergy.2016.03.093>.
- [34] S.J. Clark, M.D. Segall, C.J. Pickard, P.J. Hasnip, M.I. Probert, K. Refson, M. C. Payne, First principles methods using CASTEP, *Z. Kryst.* 220 (2005) 567–570, <https://doi.org/10.1524/zkri.220.5.567.65075>.
- [35] J.P. Perdew, K. Burke, M. Ernzerhof, Generalized gradient approximation made simple, *Phys. Rev. Lett.* 77 (1996) 3865, <https://doi.org/10.1103/PhysRevLett.77.3865>.
- [36] P.E. Blöchl, Projector augmented-wave method, *Phys. Rev. B* 50 (1994) 17953, <https://doi.org/10.1103/PhysRevB.50.17953>.
- [37] G. Kresse, D. Joubert, From ultrasoft pseudopotentials to the projector augmented-wave method, *Phys. Rev. B* 59 (1999) 1758, <https://doi.org/10.1103/PhysRevB.59.1758>.
- [38] M. Garcia-Mota, M. Bajdich, V. Viswanathan, A. Vojvodic, A.T. Bell, J.K. Nørskov, Importance of correlation in determining electrocatalytic oxygen evolution activity on cobalt oxides, *J. Phys. Chem. C* 116 (2012) 21077–21082, <https://doi.org/10.1021/jp306303y>.
- [39] W. Luo, A. Asthagiri, An ab initio thermodynamics study of cobalt surface phases under ethanol steam reforming conditions, *Catal. Sci. Technol.* 4 (2014) 3379–3389, <https://doi.org/10.1039/C4CY00582A>.
- [40] T.A. Halgren, W.N. Lipscomb, The synchronous-transit method for determining reaction pathways and locating molecular transition states, *Chem. Phys. Lett.* 49 (1977) 225–232, [https://doi.org/10.1016/0009-2614\(77\)80574-5](https://doi.org/10.1016/0009-2614(77)80574-5).
- [41] C. Gonzalez, H.B. Schlegel, An improved algorithm for reaction path following, *Chem. Phys. Lett.* 90 (1989) 2154–2161, <https://doi.org/10.1063/1.456010>.
- [42] C. Gonzalez, H.B. Schlegel, Reaction path following in mass-weighted internal coordinates, *J. Phys. Chem. A* 94 (1990) 5523–5527, <https://doi.org/10.1021/j100377a021>.
- [43] P. Bolt, F.H. Habraken, J. Geus, Formation of nickel, cobalt, copper, and iron aluminates from α - and γ -alumina-supported oxides: a comparative study, *J. Solid State Chem.* 135 (1998) 59–69, <https://doi.org/10.1006/jssc.1997.7590>.
- [44] A. Navrotsky, O. Kleppa, Thermodynamics of formation of simple spinels, *J. Inorg. Nucl. Sci.* 30 (1968) 479–497, [https://doi.org/10.1016/0022-1902\(68\)80475-0](https://doi.org/10.1016/0022-1902(68)80475-0).
- [45] H. Jo, M.K. Khan, M. Irshad, M.W. Arshad, S.K. Kim, J. Kim, Unraveling the role of cobalt in the direct conversion of CO₂ to high-yield liquid fuels and lube base oil, *Appl. Catal. B* 305 (2022), 121041, <https://doi.org/10.1016/j.apcatb.2021.121041>.
- [46] L. Wang, Y. Gao, Q. Xue, H. Liu, T. Xu, Microstructure and tribological properties of electrodeposited Ni–Co alloy deposits, *Appl. Surf. Sci.* 242 (2005) 326–332, <https://doi.org/10.1016/j.apsusc.2004.08.033>.
- [47] T. Long-Xiang, Z. Feng-Mei, Z. Lu-Bin, XPS study of nickel deposited on USY zeolites, *React. Kinet. Mech. Catal.* 57 (1996) 99–104, <https://doi.org/10.1007/BF02076126>.
- [48] Z. Zhao, W. Lu, R. Yang, H. Zhu, W. Dong, F. Sun, Z. Jiang, Y. Lyu, T. Liu, H. Du, Insight into the formation of Co@Co₂C catalysts for direct synthesis of higher alcohols and olefins from syngas, *ACS Catal.* 8 (2018) 228–241, <https://doi.org/10.1021/acscatal.7b02403>.
- [49] Q. Liu, H. Qin, J.A. Boscoboinik, G. Zhou, Comparative study of the oxidation of NiAl (100) by molecular oxygen and water vapor using ambient-pressure X-ray photoelectron spectroscopy, *Langmuir* 32 (2016) 11414–11421, <https://doi.org/10.1021/acs.langmuir.6b02752>.
- [50] Q. Wang, J. Feng, L. Zheng, B. Wang, R. Bi, Y. He, H. Liu, D. Li, Interfacial structure-determined reaction pathway and selectivity for 5-(hydroxymethyl) furfural hydrogenation over Cu-based catalysts, *ACS Catal.* 10 (2019) 1353–1365, <https://doi.org/10.1021/acscatal.9b03630>.
- [51] R. Brown, M.E. Cooper, D.A. Whan, Temperature programmed reduction of alumina-supported iron, cobalt and nickel bimetallic catalysts, *Appl. Catal.* 3 (1982) 177–186, [https://doi.org/10.1016/0166-9834\(82\)80090-0](https://doi.org/10.1016/0166-9834(82)80090-0).
- [52] N. Braidys, S. Bastien, J. Blanchard, C. Fauteux-Lefebvre, I.E. Achouri, N. Abatzoglou, Activation mechanism and microstructural evolution of a YSZ/Ni-alumina catalyst for dry reforming of methane, *Catal. Today* 291 (2017) 99–105, <https://doi.org/10.1016/j.cattod.2017.03.006>.
- [53] A. Morales-Marín, J. Ayastuy, U. Iriarte-Velasco, M. Gutiérrez-Ortiz, Nickel aluminate spinel-derived catalysts for the aqueous phase reforming of glycerol: effect of reduction temperature, *Appl. Catal. B* 244 (2019) 931–945, <https://doi.org/10.1016/j.apcatb.2018.12.020>.
- [54] A. Reynoso, J. Ayastuy, U. Iriarte-Velasco, M. Gutiérrez-Ortiz, Cobalt aluminate spinel-derived catalysts for glycerol aqueous phase reforming, *Appl. Catal. B* 239 (2018) 86–101, <https://doi.org/10.1016/j.apcatb.2018.08.001>.
- [55] Y. Ji, Z. Zhao, A. Duan, G. Jiang, J. Liu, Comparative study on the formation and reduction of bulk and Al₂O₃-supported cobalt oxides by H₂-TPR technique, *J. Phys. Chem. C* 113 (2009) 7186–7199, <https://doi.org/10.1021/jp8107057>.
- [56] W. Song, A.S. Poyraz, Y. Meng, Z. Ren, S.-Y. Chen, S.L. Suib, Mesoporous Co₃O₄ with controlled porosity: inverse micelle synthesis and high-performance catalytic CO oxidation at – 60 °C, *Chem. Mater.* 26 (2014) 4629–4639, <https://doi.org/10.1021/cm502106v>.
- [57] A. Bielański, J. Haber, Oxygen in catalysis on transition metal oxides, *Catal. Rev. Sci. Eng.* 19 (1979) 1–41, <https://doi.org/10.1080/03602457908065099>.
- [58] Y. Zheng, W. Wang, D. Jiang, L. Zhang, X. Li, Z. Wang, Ultrathin mesoporous Co₃O₄ nanosheets with excellent photo-/thermo-catalytic activity, *J. Mater. Chem. A* 4 (2016) 105–112, <https://doi.org/10.1039/C5TA07617J>.
- [59] D.R. Lide, *CRC handbook of chemistry and physics*, CRC press, 2004.
- [60] L.R. Baker, G. Kennedy, M. Van Spronsen, A. Hervier, X. Cai, S. Chen, L.-W. Wang, G.A. Somorjai, Furfuraldehyde hydrogenation on titanium oxide-supported platinum nanoparticles studied by sum frequency generation vibrational spectroscopy: acid-base catalysis explains the molecular origin of strong metal-support interactions, *J. Am. Chem. Soc.* 134 (2012) 14208–14216, <https://doi.org/10.1021/ja306079h>.
- [61] W.C. Conner Jr, J.L. Falconer, Spillover in heterogeneous catalysis, *Chem. Rev.* 95 (1995) 759–788, <https://doi.org/10.1021/cr00035a014>.
- [62] S. Velu, S.K. Gangwal, Synthesis of alumina supported nickel nanoparticle catalysts and evaluation of nickel metal dispersions by temperature programmed desorption, *Solid State Ion.* 177 (2006) 803–811, <https://doi.org/10.1016/j.ssi.2006.01.031>.
- [63] M.I. Zaki, M.A. Hasan, F.A. Al-Sagheer, L. Pasupulety, In situ FTIR spectra of pyridine adsorbed on SiO₂–Al₂O₃, TiO₂, ZnO₂ and CeO₂: general considerations for the identification of acid sites on surfaces of finely divided metal oxides, *Colloids Surf. A Physicochem. Eng. Asp.* 190 (2001) 261–274, [https://doi.org/10.1016/S0927-7757\(01\)00690-2](https://doi.org/10.1016/S0927-7757(01)00690-2).
- [64] A. Auroux, A. Gervasini, Microcalorimetric study of the acidity and basicity of metal oxide surfaces, *J. Phys. Chem. A* 94 (1990) 6371–6379, <https://doi.org/10.1021/j100379a041>.
- [65] S. Benbenek, E. Fedoryńska, P. Winiarek, Investigation of the acidity of Ni/Al₂O₃ and Ni/SiO₂–Al₂O₃ catalysts, *React. Kinet. Mech. Catal.* 51 (1993) 189–195, <https://doi.org/10.1007/BF02062495>.
- [66] D. Blackmond, E. Ko, Structural sensitivity of CO adsorption and H₂CO coadsorption on NiSiO₂ catalysts, *J. Catal.* 96 (1985) 210–221, [https://doi.org/10.1016/0021-9517\(85\)90374-4](https://doi.org/10.1016/0021-9517(85)90374-4).
- [67] K.A. Layman, M.E. Bussell, Infrared spectroscopic investigation of CO adsorption on silica-supported nickel phosphide catalysts, *J. Phys. Chem. B* 108 (2004) 10930–10941, <https://doi.org/10.1021/jp037101e>.
- [68] Y.T. Wong, R. Hoffmann, Chemisorption of carbon monoxide on three metal surfaces: nickel (111), palladium (111), and platinum (111): a comparative study, *J. Phys. Chem. A* 95 (1991) 859–867, <https://doi.org/10.1021/j100155a069>.
- [69] D. Song, J. Li, Q. Cai, In situ diffuse reflectance FTIR study of CO adsorbed on a cobalt catalyst supported by silica with different pore sizes, *J. Phys. Chem. C* 111 (2007) 18970–18979, <https://doi.org/10.1021/jp0751357>.

- [70] Y. Amenomiya, J. Chenier, R. Cvetanovic, Hydrogenation of olefins on alumina: I. Active sites for hydrogenation of ethylene, *J. Catal.* 9 (1967) 28–37, [https://doi.org/10.1016/0021-9517\(67\)90176-5](https://doi.org/10.1016/0021-9517(67)90176-5).
- [71] J. Sinfelt, Kinetics of ethylene hydrogenation over alumina, *J. Phys. Chem.* 68 (1964) 232–237, <https://doi.org/10.1021/j100784a003>.
- [72] J. Joubert, A. Salameh, V. Krakoviack, F. Delbecq, P. Sautet, C. Copéret, J. M. Basset, Heterolytic Splitting of H₂ and CH₄ on γ -Alumina as a Structural Probe for Defect Sites, *J. Phys. Chem. B* 110 (2006) 23944–23950, <https://doi.org/10.1021/jp0641841>.
- [73] J.K. Nørskov, F. Abild-Pedersen, F. Studt, T. Bligaard, Density functional theory in surface chemistry and catalysis, *PNAS* 108 (2011) 937–943, <https://doi.org/10.1073/pnas.1006652108>.
- [74] B. Hammer, J.K. Nørskov, Electronic factors determining the reactivity of metal surfaces, *Surf. Sci.* 343 (1995) 211–220, [https://doi.org/10.1016/0039-6028\(96\)80007-0](https://doi.org/10.1016/0039-6028(96)80007-0).
- [75] B. Hammer, J.K. Nørskov, Why gold is the noblest of all the metals, *Nature* 376 (1995) 238–240, <https://doi.org/10.1038/376238a0>.